Single-cell RNA-sequencing reveals immune system compartmentalization under symbiosis in the stony coral *Oculina arbuscula*

Maria Valadez-Ingersoll[1], Hanny E. Rivera[1], Jeric Da-Anoy[1], Matthew R. Kanke[2], Kelly Gomez-Campo[3, 4], M. Isabel Martinez-Rugerio[3, 4, 5], Julian Kwan[6], Ryan Hekman[6], Andrew Emili[1, 6, 7], Thomas D. Gilmore[1*], Sarah W. Davies[1*]

[1]Boston University, Department of Biology; Boston, MA, 02215, USA

[2]Amgen Research, Research Bioimics, South San Francisco, CA, 94080, USA

[3]Helmholtz-Institute for Functional Marine Biodiversity at the University of Oldenburg (HIFMB), 26129 Oldenburg, Germany

[4]Alfred Wegener Institute, Helmholtz-Centre for Polar and Marine Research (AWI), Bremerhaven, Germany

[5]Institute for Chemistry and Biology of the Marine Environment (ICBM), Carl von Ossietzky Universität Oldenburg, 26129 Oldenburg, Germany

[6]Department of Biochemistry, Boston University Chobanian & Avedisian School of Medicine, Boston, MA, 02118, USA

[7]Division of Oncological Sciences, Knight Cancer Institute, Oregon Health & Science University, portland, OR, 97201, USA

*Corresponding authors

Send correspondence to:
Sarah W. Davies, Boston University, Department of Biology, 5 Cummington Mall, Boston, MA 02215; email: daviessw@bu.edu
Thomas D. Gilmore, Boston University, Department of Biology, 24 Cummington Mall, Boston, MA 02215; email: gilmore@bu.edu

ABSTRACT

Many cnidarians host single-celled algae within gastrodermal cells, yielding a mutually beneficial exchange of nutrients between host and symbiont, and dysbiosis can lead to host mortality. Previous research has uncovered symbiosis tradeoffs, including suppression of the NF-κB immune pathway in cnidarians hosting intracellular algae and correlations between symbiotic state and pathogen susceptibility. Here, we used a multiomic approach to characterize symbiotic states of the facultatively symbiotic coral *Oculina arbuscula* by generating genotype-controlled fragments of symbiotic and aposymbiotic tissue. Metabarcoding of 16S rRNA showed no difference in bacterial communities between symbiotic states. Consistent with previous whole-organism RNA-seq studies, whole-organism proteomics revealed differential abundance of proteins related to immunity, consistent with immune suppression during symbiosis. Moreover, single-cell RNAseq identified diverse cell clusters within six cell types across symbiotic states. Specifically, the gastrodermal cell cluster containing algal-hosting cells from symbiotic tissue had higher expression of nitrogen cycling and sugar transport genes than gastrodermal cells from aposymbiotic tissue. Furthermore, lower expression of genes involved in immune regulation, including NF-κB pathway genes, was observed in these gastrodermal cells from symbiotic tissue. However, no differences in gene expression in the immune cell cluster were observed between symbiotic states. This work reveals a compartmentalization of immune system suppression in specific gastrodermal cells in symbiosis, which likely limits symbiosis tradeoffs by dampening immunity in algal hosting cells while still maintaining general organismal immunity.

KEY WORDS: coral, Oculina arbuscula, symbiosis, immunity, single-cell RNA-sequencing, proteomics

60 **INTRODUCTION**

61 Symbioses exist across the tree of life along a spectrum from parasitisms – in which one symbiotic
62 partner benefits at the cost of the other partner – to mutualisms – in which both partners benefit
63 from the relationship (1). Endosymbioses, symbiotic relationships where one organism resides
64 within another, pose immunity challenges to hosts as they must differentiate between self,
65 mutualistic symbionts, and pathogens (2,3). In mutualisms, the host immune system must be
66 regulated in order to allow for the existence of the endosymbiont (4), whereas in parasitisms the
67 endosymbiont must evade detection by the host's immune system (5). Additionally, in mutualisms,
68 hosts must tightly regulate the density of their symbionts in order to prevent overcrowding, which
69 could lead to a shift from mutualism to parasitism (2,6,7).

70 Reef-building corals participate in a mutually beneficial symbiosis with algae that reside
71 inside their gastrodermal cells, wherein the algae carry out photosynthesis and translocate fixed
72 carbon sugars to the host (8,9). In return, the host provides carbon, as well as nitrogen and
73 phosphorus species, to the symbiont (10,11). Translocation of nitrogen from the host to the
74 symbiont has been proposed as a mechanism to promote nutrient exchange while controlling algal
75 proliferation via nitrogen limitation to prevent overcrowding (6). In this hypothesized model, as
76 symbiont densities increase, the greater nutrient requirements of the algae lead to resource
77 competition between symbionts and with the host (12). In support of this hypothesis, whole-
78 organism RNA-sequencing has revealed differences in the expression of genes involved in sugar
79 transport and nitrogen cycling across cnidarians in and out of symbiosis (13) and enrichment of
80 nitrogen deprivation genes in algae exhibiting greater cell densities when associated with the sea
81 anemone *Exaiptasia pallida* (6). These whole organism studies reflect the importance of carbon
82 and nitrogen transport between symbiotic partners in the maintenance of this symbiosis.

83 In stony corals, environmental change can lead to loss of the algal symbiont in a process
84 termed coral bleaching (14). If prolonged, this dysbiosis can lead to host mortality. Since this
85 symbiotic relationship in corals is often obligate, it is challenging to separate the effects of
86 dysbiosis from nutritional loss (15). In contrast to obligate symbioses, facultatively symbiotic hosts
87 can exist in an aposymbiotic state (without or with few algal symbionts) and can buffer nutrient
88 loss through heterotrophy, allowing for studies of the influence of symbiosis on host molecular
89 function, especially in regards to nutrition and immunity (13,15–18). The sea anemone *E. pallida*
90 is a facultatively symbiotic cnidarian that has served as an instrumental model for uncovering how
91 the host immune system is fine-tuned in the presence of the algal symbiont (19,20). Additionally,
92 facultatively symbiotic stony corals, such as *O. arbuscula* (13) and *Astrangia poculata* (21), are
93 emerging as models for studying these processes in calcifying cnidarians.

94 Research using these facultatively symbiotic models has identified specific pathways
95 within the host immune system as key for the cnidarian-algal symbiosis. For example, activation
96 of pathways associated with the transcription factor (TF) NF-κB have been implicated in immunity
97 across metazoans, and this TF is downregulated in symbiotic compared to aposymbiotic hosts
98 (13,19). Additionally, the attenuation of immune pathways associated with symbiosis has been
99 suggested to affect organismal immunity (22). However, this dampening of immunity is not always
100 correlated with increased susceptibility to pathogen challenges (23,24). For example, recent work
101 has shown that the NF-κB pathway can be independently modulated by cnidarians capable of
102 symbiosis under energetic limitation (25). Additionally, many antioxidant and oxidative response
103 pathways are constitutively higher in symbiotic compared to aposymbiotic cnidarians (26). A
104 nuanced picture of the symbiotic cnidarian immune system has emerged, with questions remaining

105 on how the immune system is regulated under endosymbiosis without compromising whole-
106 organism immunity.

107 Here, we used a multiomic approach to explore symbiosis-immunity tradeoffs in the
108 facultatively symbiotic coral *O. arbuscula*. Whole organism proteomics confirms broad immune
109 dampening in symbiosis. Based on single-cell RNA-seq of genotype-controlled fragments, we
110 profiled the cellular diversity of *O. arbuscula* under different symbiotic states to determine how
111 tradeoffs of endosymbiosis and immunity manifest by rewiring gene expression across different
112 cell states. Strikingly, we found that gene expression differences in immune pathways occur in
113 gastrodermal cells that host algae. These results suggest that cell state-specific dampening of
114 immunity explains how some symbiotic organisms balance the immune tradeoffs of symbiosis
115 with the maintenance of organismal immunity.

116

117 **MATERIALS AND METHODS**

118 Detailed information on sample preparations, bioinformatic analyses, and R packages can be found
119 in the Supplemental Materials.

120

121 **Coral husbandry and manipulation of symbiotic state**

122 Symbiotic (in symbiosis with *Brevioulum psygmophilum*) (27) colonies from seven genetic
123 backgrounds (genets A-G) of *Oculina arbuscula* were collected at Radio Island Jetty, North
124 Carolina and have been maintained at Boston University (BU) in common garden aquaria since
125 May, 2018. Aposymbiotic branches were generated via menthol bleaching. Aposymbiotic status
126 was confirmed by a lack of symbiont autofluorescence under fluorescence microscopy (Leica

127 M165 FC), and aposymbiotic branches were transferred back to common garden aquaria and
128 maintained for at least 2 months of recovery prior to physiological and multiomic profiling.
129

130 **Tissue removal and symbiont cell quantification**

131 To measure symbiont cell densities in symbiotic and aposymbiotic *O. arbuscula*, small branches
132 were fragmented from symbiotic (N=10) and aposymbiotic (N=10) samples from five genets.
133 Tissue was removed via airbrushing, homogenized, and symbiont counts were normalized to
134 skeletal surface area using an Einscan-SE scanner. Statistical differences between symbiotic and
135 aposymbiotic fragments were calculated using the Kruskal-Wallis rank sum test, as assumptions
136 of normality were not met.
137

138 **Coral spectroscopic determinations**

139 Light absorption capacities of symbiotic and aposymbiotic *O. arbuscula* were compared using
140 reflectance and absorptance (28–30). Coral reflectance (R), the fraction of light reflected, was
141 measured between 400-750 nm in intact fragments using a miniature spectroradiometer (Flame-T-
142 UV-Vis, Ocean Optics Inc.). Reflectance was expressed as the ratio of the measurement from the
143 tissue surface relative to the reflectance of a bleached *O. arbuscula* skeleton. Coral absorptance
144 (A), which describes the fraction of incident light absorbed by coral tissue, was calculated from
145 the reflectance spectra as $A = 1 – R$ (28,30). The absorptance peak of chlorophyll a (Chl a) at 675
146 nm was calculated as $A_{675} = 1 – R_{675}$, assuming that transmission through the skeleton is negligible.
147

148 **Bacterial community profiling**

149 To identify bacterial communities associated with symbiotic and aposymbiotic fragments, one
150 symbiotic and one aposymbiotic fragment from five genotypes were flash frozen, and a subsample
151 was preserved in ethanol for 16S metabarcoding (N=10). Metabarcoding libraries were generated
152 using a series of PCR amplifications for the V4/V5 region of the bacterial 16S rRNA gene (31,32).
153 Five negative controls were prepared and used to remove contaminating sequences. Samples were
154 sequenced on an Illumina MiSeq at Tufts University Core Facility (paired-end 250 bp).

155 16S read processing inferred 661 amplicon sequence variants (ASVs) with assigned
156 taxonomy across samples. Bacterial communities across symbiotic states were compared via alpha
157 diversity (Shannon index, Simpson's index, ASV richness, and evenness) and beta diversity
158 (PCoA with Bray–Curtis dissimilarities). Alpha diversity metrics were compared using linear
159 mixed effects models with symbiotic state as the predictor and a random effect of genotype. The
160 effect of symbiotic state on beta diversity was assessed using the function betadisper (vegan
161 package; v2.6-4 (33)). DESeq2 v1.40.2 (34) explored differentially abundant ASVs to ensure that
162 subtle differences in specific taxa were not overlooked.

163

164 **Proteomic profiling**

165 Mass spectroscopy (MS) was used to identify differentially enriched proteins from total protein
166 isolated from fragments of four symbiotic genets and three aposymbiotic genets. Total protein was
167 isolated as described previously (35) and stored at -80 ℃.

168 For MS, tryptic peptide mixtures were analyzed by nano-scale high-performance liquid
169 chromatography (Proxeon EASY-Nano system, Thermo Fisher Scientific) coupled with online
170 nanoelectrospray ionization tandem MS (Q-Exactive HF-X mass spectrometer; Thermo Fisher
171 Scientific) (36). For protein identification and analysis, data files were searched using the standard

172 workflow of MaxQuant version 2.4 (http://www.maxquant.org/) under standard settings using
173 concatenated genomes of *Astrangia poculata* (21) and *Fungia* sp. (37). A false discovery rate
174 (FDR) threshold of 1% was used to filter candidate peptides and protein identifications. Following
175 data filtration, normalization, and clustering with Omics Notebook (38), 2,730 proteins were
176 retained. Differential abundance analysis of proteomic profiles between aposymbiotic and
177 symbiotic samples was based on a moderated t-test (38) in which proteins were considered
178 differentially abundant if they had a Bonferroni adjusted p-value < 0.1. Raw intensity counts were
179 *rlog*-normalized in DESeq2 (34) and visualized using a Principal Component Analysis (PCA)
180 using vegan v2.6-4 (33). Effects of symbiotic state and genet were assessed using PERMANOVA
181 with the adonis2 function in vegan v2.6-4 (33). Predicted *O. arbuscula* peptides were searched
182 against the human proteome v.11.5 from the STRING v.11 database (39) with an e-value cut-off
183 of $1x10^{-5}$. Protein–protein interactions of select differentially expressed proteins (FDR < 0.1) were
184 retrieved from the STRING v.11 database (39). Interaction networks were visualized using
185 Cytoscape v.3.7.2 (40).
186

187 **Single-cell RNA-sequencing**

188 To create single-cell libraries, one symbiotic and one aposymbiotic branch of *O. arbuscula*
189 genotype F were sampled for single-cell isolation and 10X cDNA sequencing (41). Cell isolation
190 samples were analyzed by BU's Single Cell Sequencing Core Facility. The symbiotic sample had
191 a concentration of 2,625 cells/µl and viability of 81.6%. The aposymbiotic sample had a
192 concentration of 3,313 cells/µl and viability of 86.4%.

193 Libraries were generated following the 10X Genomics Chromium Single Cell 3'v3
194 protocol, and quality was assessed via a Bioanalyzer. Samples were pooled in equimolar

concentration and sequenced on an Illumina NextSeq 2000 (P3 100 kit) with a target of 50,000 reads per cell. CellRanger (v7.2.0 (42)) processed reads, which were aligned to concatenated genomes of *Astrangia poculata* (21) and the algal symbiont *Breviolum psygmophilum* (13). Only reads that aligned confidently to the host reference were used to generate CellRanger output files.

Following alignment, host reads from symbiotic and aposymbiotic samples were analyzed using Seurat (v.5.0.2) (43). Datasets were cleaned (genes expressed in fewer than three cells were discarded, as were cells expressing fewer than 200 genes), normalized, and scaled, and a PCA reduction was performed. Datasets were integrated using the Canonical Correlation Analysis (CCA) Integration method on the PCA reduction of the top 2,000 most variable genes (nearest neighbors parameters). Cell clusters were identified using 30 dimensions (resolution: 0.5) and visualized using Uniform Manifold Approximation and Projection (UMAP). Marker genes for each cluster were identified using FindAllMarkers (Wilcoxin Rank Sum Test; log-fold-change threshold: 0.5) and compared to genes expressed highly in cell types from other cnidarian single-cell datasets (Supplementary Dataset 1) (44,45). 28 cell clusters across 6 cell types were identified in the UMAP and characterized using marker genes and previous scRNA-seq datasets in the corals *Stylophora pistillata* (44) and *Xenia* sp. (45). Proportions of each cell cluster within each library were calculated (number of cells in each cluster divided by total number of cells). Broad transcriptomic differences between cell clusters were assessed by identifying the top 10 genes enriched in each cluster compared to all other clusters.

To compare expression profiles of specific cell states between symbiotic and aposymbiotic samples, cell clusters of interest were independently reclustered, and the effect of symbiotic state on gene expression in each cell state was analyzed. First, the cell cluster of interest (*e.g.,* Immune Cell, Gastrodermis 1) was subsetted and new variable features were identified. Data were rescaled,

218 and dimensionality reduction was re-run (first 30 dimensions). Subclusters were identified with
219 resolutions of 0.5 (Immune Cell) and 0.25 (Gastrodermis 1). The distribution of cells across
220 subclusters between symbiotic states was visualized using a UMAP. In Gastrodermis 1 and
221 Immune Cell clusters, proportions of each subcluster within each library were calculated.
222 Differentially expressed genes between symbiotic states in Immune Cell and Gastrodermis 1 cell
223 clusters were identified using DESeq2 in the FindMarkers function. Additionally, marker genes
224 for each subcluster were identified. To highlight differences in the transcriptomes of the Immune
225 Cell states, the top 20 genes enriched in each Immune Cell subcluster were identified and plotted
226 (unannotated genes were removed).

227 To compare expression of genes involved in sugar transport and nutrient cycling in
228 gastrodermal cells between symbiotic aposymbiotic states, expression of these genes in the
229 reclustered Gastrodermis 1 cells was analyzed. Normalized expression values of genes involved
230 in nitrogen cycling/symbiont density control (Glutamate Dehydrogenase DHE4 and Glutamate
231 Synthase [NADH] GLSN) and sugar transport (Apolipophorin APOB.1) (13) were compared
232 across each subcluster. FeaturePlot then visualized co-expression of these genes across the
233 subclusters of Gastrodermis 1 cells from the symbiotic sample (scaling the per-cell mean
234 expression to a maximum value of 10).

235 Finally, to identify genes driving separation between symbiotic states within the
236 Gastrodermis 1 cluster, the distribution of Gastrodermis 1 cells was visualized along the first 10
237 PCs of the PCA assay used to define the Gastrodermis 1 UMAP. An analysis of variance
238 determined whether Gastrodermis 1 cells separated by symbiotic state (symbiotic vs.
239 aposymbiotic) along each PC. The top 20 genes driving the distribution of cells along the first 7
240 PCs (10 genes driving each PC in the positive direction and 10 genes driving each PC in the

241 negative direction) were selected, and unannotated genes were removed leaving a total of 86
242 remaining genes. DESeq2 $\log_2$foldchange values with accompanying *p*-adjusted values (<0.05) for
243 each of these genes were plotted in a bar graph, and genes hypothesized to be involved in the NF-
244 κB pathway were noted. Normalized expression values of Heat Shock Factor 90 (H90A1),
245 Cathepsin L (CATL.6), Cathepsin Z (CATZ), Matrix Metallopeptidase 25 (MMP25), and Glucose-
246 Regulated Protein 78 (GRP78) were compared between symbiotic and aposymbiotic cells in the
247 Gastrodermis 1 cell cluster. Distributions of these genes across Gastrodermis 1 cells from
248 symbiotic and aposymbiotic samples were further visualized to emphasize the reduction in certain
249 immune pathways in predicted algal-hosting cells (FeaturePlot; minimum normalized expression
250 value plotted for H90A1=3, and minimum normalized expression value plotted for CATL.6,
251 CATZ, MMP25, and GRP78=2).
252
253 **RESULTS**
254 For the following experiments, genetically controlled symbiotic and aposymbiotic fragments of *O.*
255 *arbuscula* were used. Symbiotic fragments had symbiont densities that were 400-fold greater
256 (13,678 +/- 6,204 cells/cm^2) than those of aposymbiotic fragments (30 +/- 43 cells/cm^2) ($p<0.001$)
257 (**Fig. 1a**). These fragments were then used to generate light-absorption profiles, 16S rRNA
258 metabarcoding libraries, tissue proteomics, and single-cell RNA-sequencing profiles.

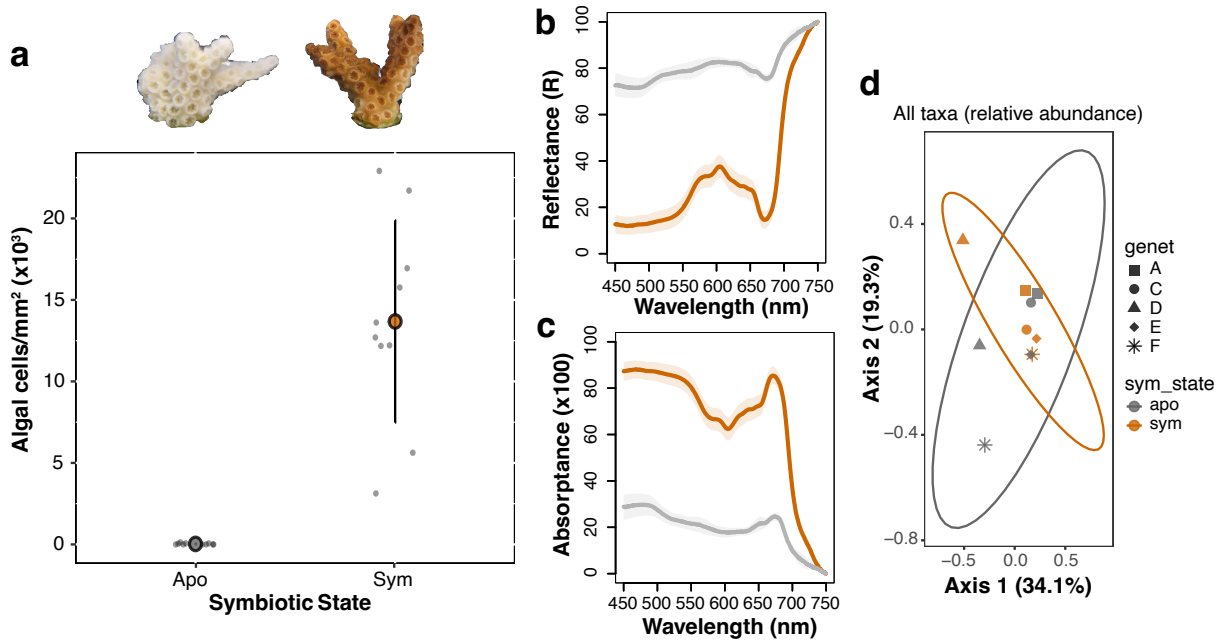

Fig. 1 Symbiosis facilitates higher light absorptance but no changes to bacterial communities in *O. arbuscula*. a Algal cell counts are 400x higher in symbiotic (brown, right) *O. arbuscula* fragments than in aposymbiotic (white/gray, left) fragments ($p<0.001$). **b** Average reflectance (R) in the PAR region (400–700 nm) was 22% +/- 4% in symbiotic *O. arbuscula* (brown) and 77% +/- 3% in aposymbiotic *O. arbuscula* (gray) ($p < 0.01$). **c** Average absorptance (A) (A = 1-R) demonstrating relative amount of solar energy with potential for use in photosynthesis. Symbiotic *O. arbuscula* (brown) has an A_{675} of 85% (+/- 4%), suggesting a functional symbiosis, and aposymbiotic (gray) has an A_{675} of 24% (+/- 2%) ($p<0.001$). In **b** and **c**, shaded colored areas represent standard deviation. **d** PCoA of bacterial communities from all ASVs in 16S data from symbiotic (brown) and aposymbiotic (gray) *O. arbuscula* genotypes. No differences in bacterial communities were observed between symbiotic states.

Light absorption is higher in symbiotic *O. arbuscula*

Differences in symbiont cell densities induced significant differences in *in vivo* coral light absorption. Reflectance spectra measurements and absorption properties of intact corals showed significant pigment content differences between symbiotic and aposymbiotic *O. arbuscula*. Average reflectance in the PAR region (400–700 nm) of symbiotic fragments was 22% +/- 4%, whereas aposymbiotic coral reflectance was 77% +/- 3% ($p < 0.01$) (**Fig. 1b**). In symbiotic fragments, the absorptance value at the peak for Chlorophyll a (A_{675}) was 85% +/- 4%, compared

279 to 24% +/- 2% in aposymbiotic samples (p<0.0001) (**Fig. 1c**). Absorptance describes the relative
280 amount of solar energy/incident light that can potentially be used in photosynthesis for organic
281 carbon fixation.
282
283 **Bacterial communities do not differ across symbiotic states**
284 We profiled the bacterial communities of aposymbiotic and symbiotic fragments from 5 genets
285 (N=10). A total of 208,330 sequences were acquired with a mean depth of coverage of 20,833 +/-
286 16050.23 per sample (Table S1). Sample rarefication yielded a total of 8,298 reads per sample
287 with a total of 661 ASVs identified across samples. No differences in bacterial communities were
288 observed between symbiotic and aposymbiotic fragments (**Fig. 1d**), and both states were
289 dominated by Proteobacteria and Bacteroidota (**Fig. S1**). Additionally, no differences in alpha
290 diversity were observed between symbiotic states regardless of the metric tested, nor were
291 differences in beta diversity by symbiotic state detected (**Fig. S2a-d**). DESeq2 tested for
292 differentially abundant ASVs across symbiotic states, while modeling genetic background, but no
293 ASVs were identified.
294
295 **The proteome is affected by symbiotic state in *O. arbuscula***
296 To compare proteomes of symbiotic and aposymbiotic *O. arbuscula*, we performed mass
297 spectrometry on whole-cell lysates from coral fragments. We identified a total of 2,929 proteins
298 in *O. arbuscula*, 2,730 of which were retained following filtering. PCA showed that samples
299 clustered by symbiotic state (p_{state}<0.05) and genet (p_{genet}<0.001) (**Fig. 2a**). A total of 281 proteins
300 were differentially enriched across symbiotic states (*p*-adjusted<0.1): 163 proteins were enriched
301 in symbiotic *O. arbuscula*, 118 proteins were enriched in aposymbiotic *O. arbuscula* (**Figs. 2b-c**).

Differentially enriched proteins (DEPs) were assigned functional categories based on a homology search of each DEP sequence in the UniProtKB database (evalue < 1×10^{-5}). DEPs involved in Immune Response, Apoptosis, Wound Healing, Oxidative Stress, Metabolic Process, and Development were identified (**Fig. 2d**)

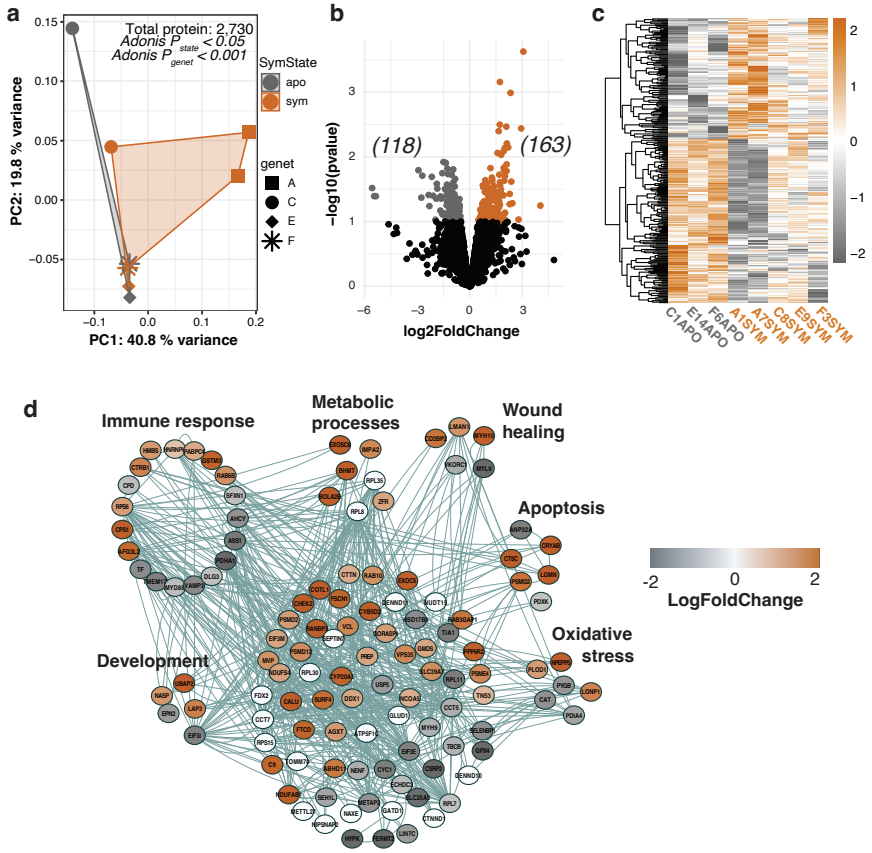

Fig. 2 Proteomic profiles of symbiotic and aposymbiotic *O. arbuscula* reveals differential enrichment of proteins by symbiotic state. a Principal component analysis of proteomic profiles across four genets, with symbiotic (sym) and aposymbiotic (apo) states distinguished by color, and genets by shape. **b** Volcano plot of differentially enriched proteins (DEPs) identified through pairwise comparison (p-value < 0.1). Proteins enriched in symbiotic samples (163) are represented by brown dots, proteins enriched in aposymbiotic samples (118) by gray dots, while black dots indicate non-DEPs in symbiotic relative to aposymbiotic corals (total N=2,730). **c** Heatmap of all DEPs across symbiotic states of *O. arbuscula*. The color scale represents the $\log_2$foldchange of each protein (row) for each coral sample (column) relative to the protein's mean across all samples. **d** Interaction network of proteins associated with immune response, metabolism, wound healing, apoptosis, oxidative stress, and development, derived from human protein–protein interactions in the STRING database. Node colors indicate upregulation (brown) or downregulation (gray) in symbiotic coral samples.

320
321 **Single-cell RNA-seq identifies cell states shared between symbiotic and aposymbiotic *O.***
322 ***arbuscula***

323 To profile gene expression in different cell types and states from symbiotic and aposymbiotic *O.*
324 *arbuscula*, we used the 10X single-cell RNA-sequencing (scRNA-Seq) platform. We captured a
325 total of 6,956 cells (3,136 cells from the symbiotic sample; 3,820 cells from the aposymbiotic
326 sample), with an average of 158,426 reads per cell, 1,113 median UMI counts per cell, and 645
327 median genes per cell. Quality control data for both samples are summarized in Supplementary
328 Dataset 2. 6,942 cells were retained following filtering (3,192 cells from the symbiotic sample;
329 3,813 cells from the aposymbiotic sample).

330 Clustering of the integrated 10X gene expression datasets from the filtered symbiotic and
331 aposymbiotic samples resulted in the identification of 28 transcriptomically distinct cell clusters
332 across six broad cell types (**Fig. 3a)**. Cells from symbiotic and aposymbiotic samples were
333 represented in all clusters, although some clusters had different cell proportions across samples.
334 For example, symbiotic cells identified in Gastrodermis 1 represented a slightly larger percentage
335 (19.8%) of the total symbiotic library than in the aposymbiotic library (15.5%) (**Fig. 3b**).
336 Additionally, each cluster defined in the UMAP displayed distinct transcriptomic programming as
337 exemplified by expression patterns of the ten highest enriched genes in each cluster (**Fig. 3c**).

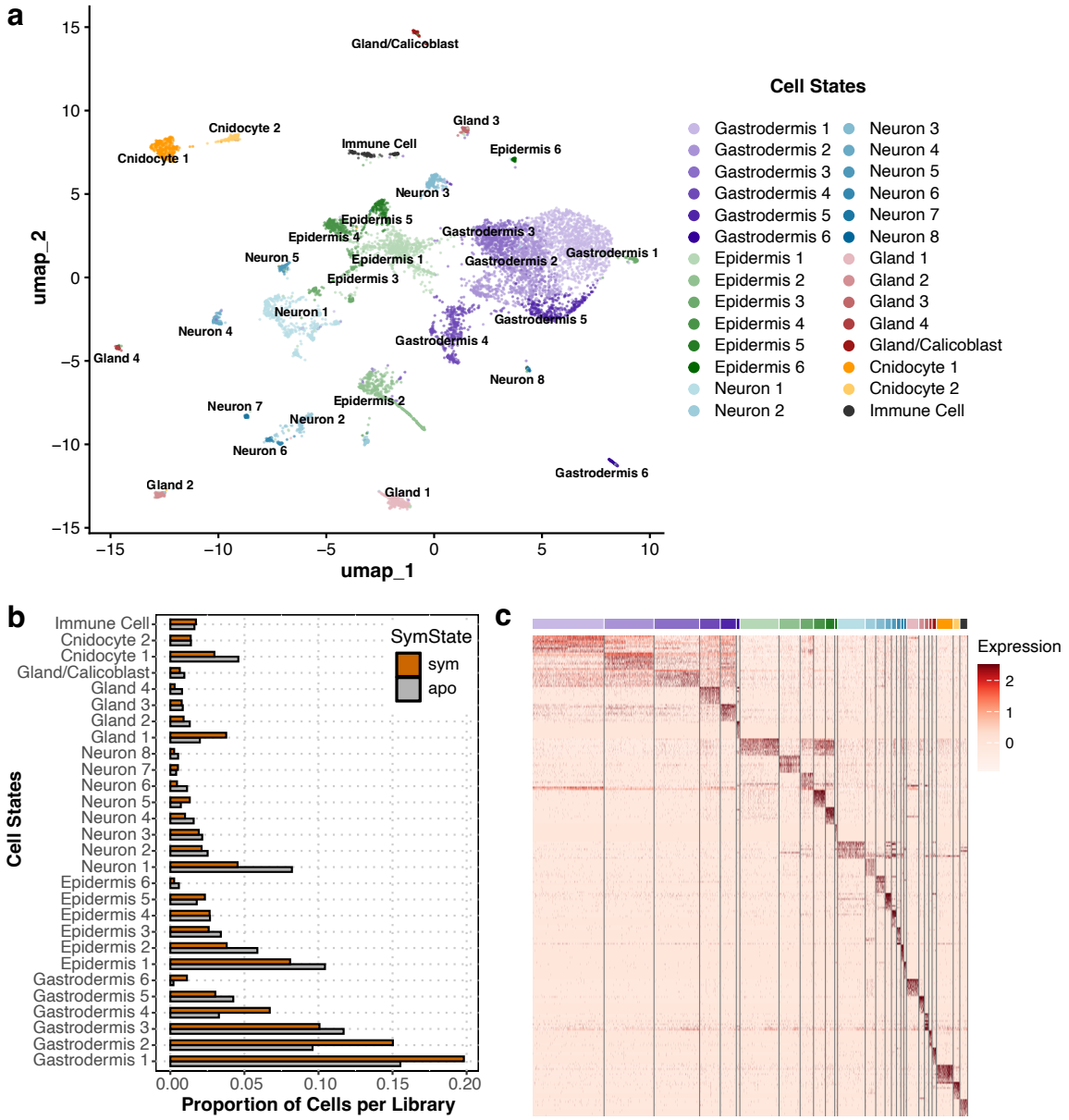

Fig. 3 scRNA-seq reveals 28 transcriptomically distinct cell clusters across 6 cell types in symbiotic and aposymbiotic *O. arbuscula*. **a** A UMAP Projection of the transcriptomes of 6,942 cells from symbiotic (sym) and aposymbiotic (apo) *O. arbuscula* reveals 28 clusters across 6 broad cell types. Each cluster is color coded. **b** Proportions of clusters per library across all cell states in aposymbiotic and symbiotic samples. **c** Each cluster is transcriptomically distinct, with transcriptomic similarities present between clusters of the same cell type, as represented by the 10 genes most highly expressed in each cluster. Expression values are average $\log_2$foldchanges computed from normalized gene expression data of each cell. Cell clusters are colored as in (**a**).

350 **Identification of symbiont-hosting gastrodermal cells**

351 To investigate gene expression differences between gastrodermal cells from symbiotic compared
352 to aposymbiotic *O. arbuscula*, we subsetted and reclustered cells from each of the six
353 Gastrodermal states. Four subclusters were revealed within Gastrodermis 1, suggesting additional
354 cell states (**Fig. 4a**). Gastrodermis 1 Subcluster 2 was composed almost entirely of cells from the
355 symbiotic sample (**Fig. 4b**).

356 To predict the localization of the symbiont-hosting cells within our dataset, we selected
357 sugar transport and nitrogen cycling genes, which have been previously shown to have higher
358 expression in symbiotic compared to aposymbiotic *O. arbuscula* (13). DESeq2 identified
359 differences in gene expression in gastrodermal cells between symbiotic and aposymbiotic samples,
360 which showed that Gastrodermis 1 cells from symbiotic *O. arbuscula* had overexpression of genes
361 related to nitrogen cycling (Glutamate Dehydrogenase DHE4 and Glutamate Synthase [NADH]
362 GLSN) and sugar transport (Apolipophorin APOB.1) (p-adjusted <0.05) (**Fig. 4c-e**). Furthermore,
363 DHE4, GLSN, and APOB.1 were identified as marker genes for Subcluster 2 (indicating that these
364 genes were expressed higher inside than outside Subcluster 2 (p-adjusted <0.05; **Fig. 4f-h**).
365 Additionally, there was strong co-expression of these symbiosis-marker genes in Subcluster 2,
366 suggesting that this cell state is actively transporting fixed carbon sugars while mediating the
367 growth and division of the hosted algal symbionts (**Fig. 4i-k**). There was little co-expression of
368 these genes in Subclusters 1, 3, and 4 of Gastrodermis 1, suggesting that non-symbiont-hosting
369 gastrodermal cell states perform nitrogen and carbon sugar processing independently or through
370 distinct pathways. The presence of a symbiotic-only subcluster within Gastrodermis 1 and the co-
371 expression of highly expressed markers for symbiosis within this subcluster indicated that

Subcluster 2 of Gastrodermis 1 comprised the algal-hosting gastrodermal cell state from the symbiotic sample.

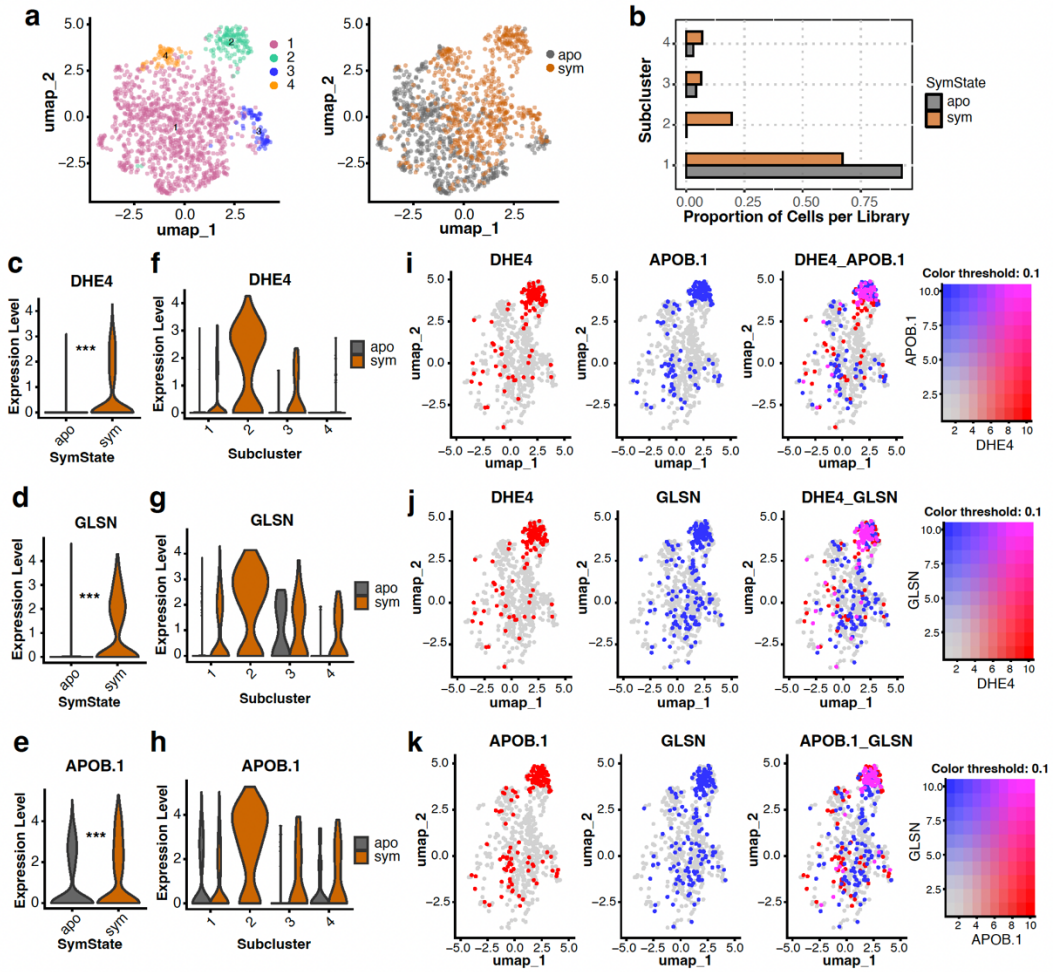

Fig. 4 The Gastrodermis 1 cell cluster contains symbiont-hosting cells and is involved in sugar transport and nitrogen cycling. a UMAP projections of the 1,212 independently reclustered Gastrodermis 1 cells revealed 4 subclusters. Each subcluster is color-coded in the left panel. Gastrodermis 1 cells separate according to symbiotic state across the UMAP projection (right panel). **b** Subclusters represented different proportions of the total Gastrodermis 1 symbiotic and Gastrodermis 1 aposymbiotic libraries, most notably in Subcluster 2. Glutamate Dehydrogenase (DHE4, **c**), Glutamate Synthase [NADH] (GLSN, **d**), and Apolipophorin (APOB.1, **e**) were more highly expressed in Gastrodermis 1 cells from symbiotic compared to aposymbiotic *O. arbuscula*. *** denotes *p*-adjusted value < 0.001. DHE4 (**f**), GLSN (**g**), and APOB.1 (**h**) were identified as marker genes for Subcluster 2. Expression levels of genes in **c-h** are normalized per cell, and significance is calculated from DESeq2. Coexpression plots of DHE4 and APOB.1 (**i**), DHE4 and GLSN (**j**), and APOB.1 and GLSN (**k**) across Gastrodermis 1 cells from symbiotic *O. arbuscula* revealed high coexpression of these sugar transport and nitrogen cycling genes within Subcluster 2, but not in the other subclusters. The coloration of each cell represents the per-cell mean expression value of each gene scaled to a maximum value of 10.

390 **No differences identified in immune cell gene expression between symbiotic states**

391 To determine whether downregulation of the immune system observed in whole-organism studies
392 of symbiotic compared to aposymbiotic coral (13) was observed in the relative proportions of
393 immune cells or in cell-state gene expression, we identified one Immune Cell cluster in our single-
394 cell dataset (**Fig. 5a**). This cluster contained approximately equal proportions of cells from both
395 symbiotic (47%) and aposymbiotic (53%) samples, and, after subsetting and independently
396 reclustering these Immune Cells, we identified three cell states with distinct transcriptomic profiles
397 (**Fig. 5b**). However, cells did not cluster by symbiotic state after reclustering and no differential
398 expression between Immune Cells from symbiotic and aposymbiotic samples was observed (*p*-
399 adjusted <0.05; **Fig. 5c**). These similarities in relative proportions and gene expression of
400 symbiotic and aposymbiotic Immune Cells indicated that this cell cluster is not responsible for
401 whole-organism differences in immunity, but the identification of three distinct subclusters
402 (immune cell states) are indicative of diversified immune cell functions in *O. arbuscula* that are
403 independent of symbiotic state.

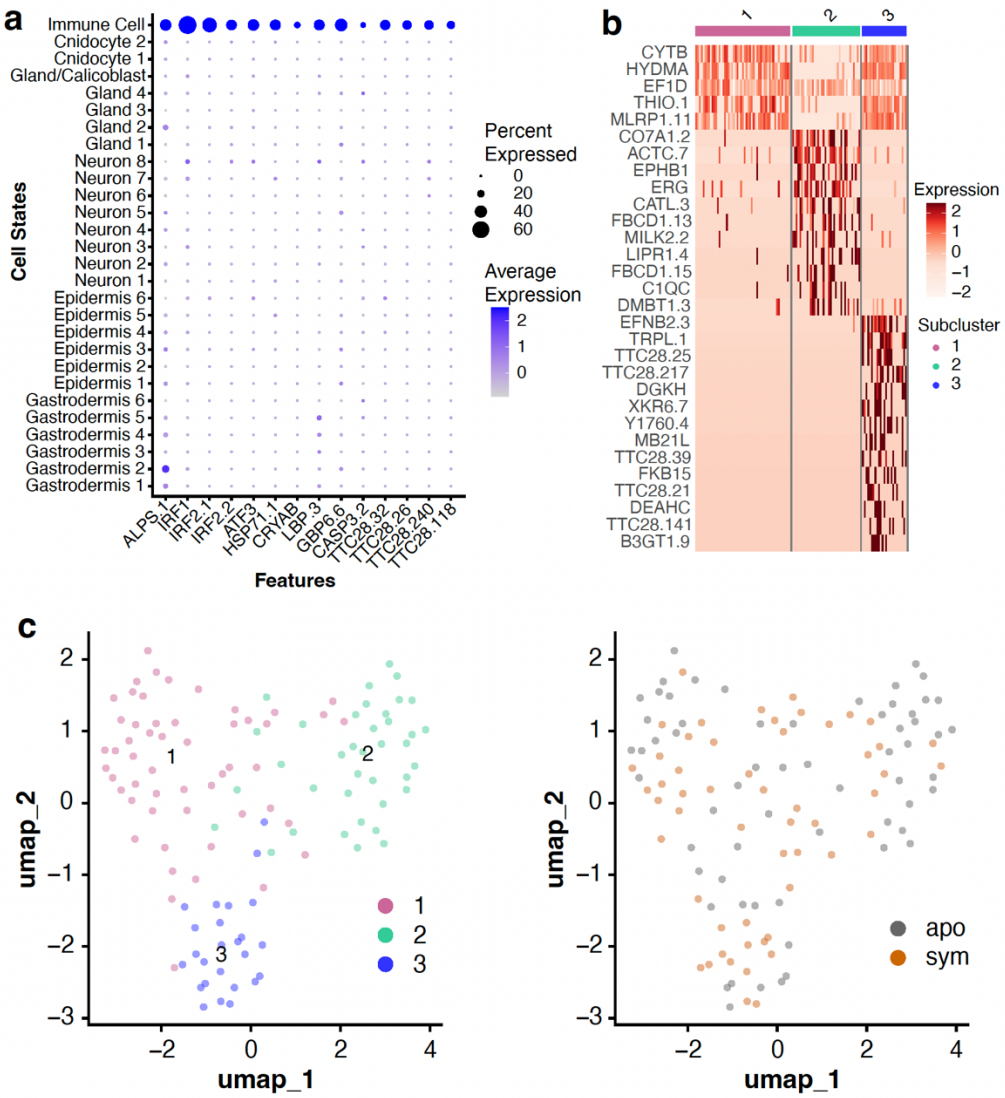

Fig. 5 No gene expression differences between Immune Cells of symbiotic and aposymbiotic samples. a The Immune Cell cluster has high expression of previously identified immune cell marker genes. Dot size represents the percentage of cells in each cell state that express each gene, and dot color represents the average (normalized) expression level of each gene within each cell state. **b** Three Immune Cell subclusters have distinct transcriptomic profiles, as represented by the annotated genes within the top 20 most highly enriched genes in each subcluster. Expression values are average $\log_2$foldchanges computed from normalized gene expression data of each cell. **c** UMAP projections of the 116 independently reclustered Immune Cells revealed 3 subclusters (left panel) that do not separate according to symbiotic state (right panel).

Immune response genes are downregulated in symbiotic Gastrodermis 1 cells

Because the Immune Cells failed to cluster by symbiotic state, but Gastrodermis 1 cells did, we determined which factors (genes) were driving this pattern in the UMAP of Gastrodermis 1 cells.

418 We analyzed the distribution of the cells along each of the first 10 Principal Components (PCs) in
419 the PCA dimensionality reduction that was used to generate the Gastrodermis 1 UMAP.
420 Gastrodermis 1 cells exhibited significant separation by symbiotic state along the first 7 PCs (*p*-
421 value < 0.05) (**Figure S3a-e**). Of the 86 annotated genes driving the distribution of cells along
422 each of the top 7 PCs, 36 were differentially expressed between Gastrodermis 1 cells by symbiotic
423 state (*p*-adjusted <0.05), and 12 of these 86 genes have been proposed to function in the NF-κB
424 pathway (**Fig. 6a**). Expression of five putative NF-κB response genes H90A (46–49), CATL.6
425 (50–52), CATZ (52), MMP25 (53), and GRP78 (54) was significantly lower in Gastrodermis 1
426 cells from symbiotic hosts (*p*-adjusted <0.05; **Fig. 6b-d, Fig. S4a-b**), and this pattern was strongest
427 in the symbiotic cells in Subcluster 2 **(Fig. 6e-g, Fig. S4c-d**). Although six other putative NF-κB
428 pathway genes were identified as drivers of cell state clustering, they were not differentially
429 expressed (TRAF3.10 (55), TNIP1 (56), SHH (57), KLF5 (58), DNAJ1 (59), and ADAM9.1 (60)).
430 PAX7 (61) was more highly expressed in Gastrodermis 1 cells from symbiotic tissue (**Fig. 6a**).
431 Regardless, the regulation of possible NF-κB pathway genes in these algal-hosting cells is clearly
432 responsible for differentiating this cell state.

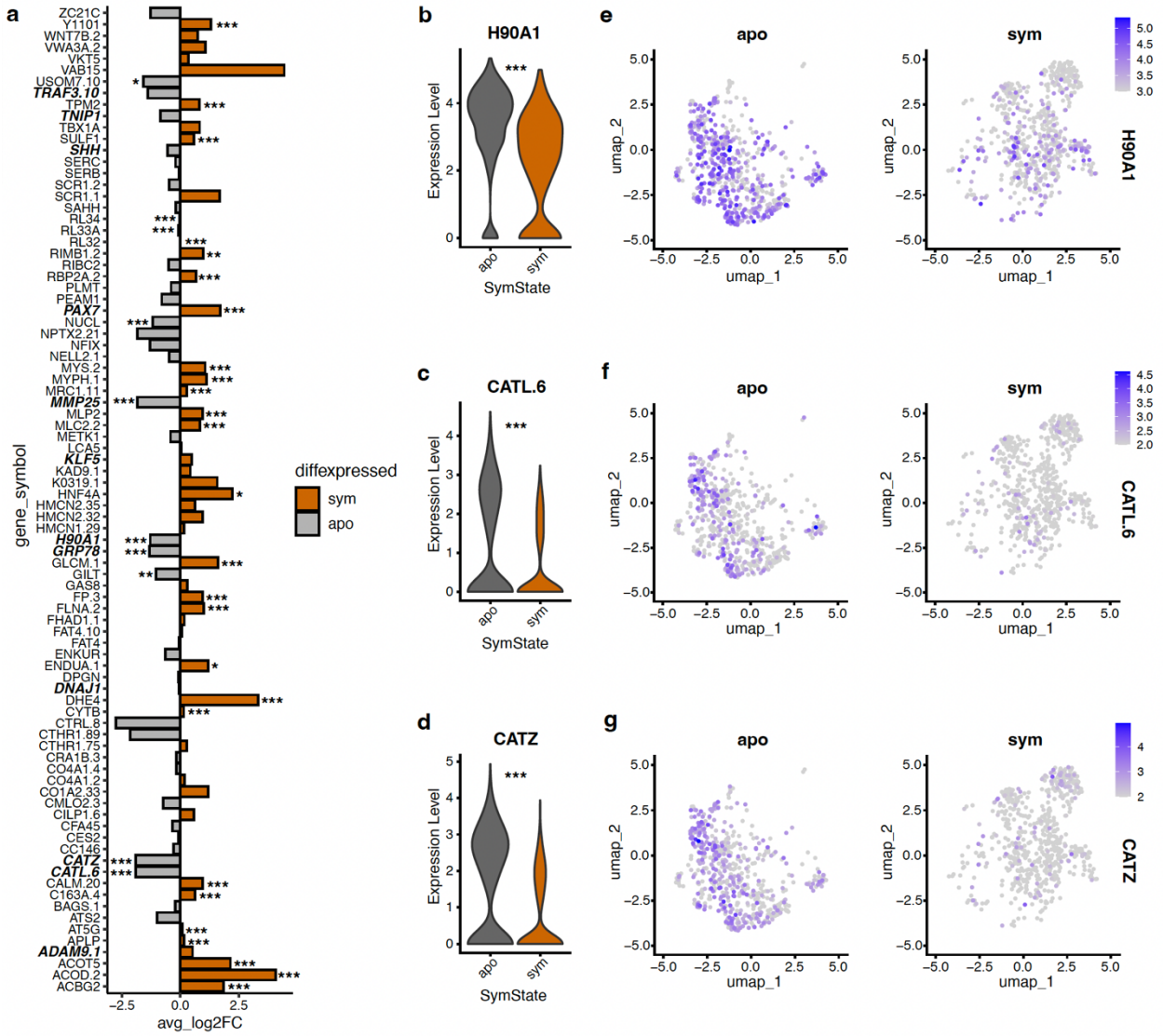

433

434 **Fig. 6 Gastrodermis 1 cells from symbiotic samples downregulate immune pathway genes**
435 **compared to aposymbiotic samples. a** 36 of the 86 annotated genes that drive Gastrodermis 1
436 cell clustering along the first 7 PCs were differentially expressed (*** = *p*-adjusted value < 0.001,
437 *** = *p*-adjusted value < 0.01, * = *p*-adjusted value < 0.05). Bold, italicized genes are hypothesized
438 to function in the NF-κB pathway. Putative NF-κB response genes Heat Shock Factor 90 (H90A1
439 **b**), Cathepsin L (CATL.6 **c**), and Cathepsin Z (CATZ **d**) were more highly expressed in
440 Gastrodermis 1 cells from aposymbiotic compared to symbiotic *O. arbuscula*. Expression levels
441 of genes in **b-d** are normalized per cell, and significance is calculated from DESeq2. Expression
442 of H90A1 (**e**), CATL.6 (**f**), and CATZ (**g**) are plotted across all symbiotic and aposymbiotic
443 Gastrodermis 1 cells. Coloration represents the normalized expression value (minimum
444 normalized expression value plotted for H90A1=3, and minimum normalized expression value
445 plotted for CATL.6 and CATZ=2).
446

447

448 **DISCUSSION**

449 Here, we have characterized how host immunity is modulated to facilitate endosymbiosis by
450 quantifying phenotypic metrics of symbiosis, by profiling bacterial communities, and by
451 performing whole-organism proteomics and single-cell RNA-sequencing (scRNA-Seq) in
452 symbiotic (with algal symbionts) and aposymbiotic (without algal symbionts) samples of the
453 facultatively symbiotic stony coral *Oculina arbuscula.* This work reveals cell state-specific
454 compartmentalization of the immune system that allows symbiotic hosts to downregulate key
455 immunity pathways in algal-containing cells while maintaining constitutive organismal immunity
456 across other cell types. Our results are consistent with emerging data indicating that the cnidarian-
457 algal symbiosis is a balancing act between nutritional status and immunity (12,13,19). Hosts must
458 balance beneficial nutrient acquisition from photosynthetic algae with the required downregulation
459 of the immune system to allow for intracellular symbiont establishment and maintenance.

460 Whole-organism transcriptomic and proteomic research has yielded many insights into
461 how symbiosis influences cnidarian host function. For example, transcriptomic (13) and proteomic
462 (ref. 62, and this study) experiments have demonstrated how symbiosis affects gene expression
463 and protein abundance. Our comparison of whole-organism proteomics between different
464 symbiotic states at baseline conditions supports previous experiments (13,19,63) suggesting that
465 differential regulation of the host immune system is required to maintain symbiosis. Specifically,
466 we observed a decrease in proteins within the NF-κB pathway in symbiotic compared to
467 aposymbiotic samples, which is consistent with gene expression patterns in *O. arbuscula* observed
468 by Rivera and Davies (13). However, signals from whole-organism studies may be confounded by
469 differences in proportions of cell types sampled and opposing expression signals within these cell
470 types (64).

471 scRNA-seq has been gaining traction in research on the coral immune system. In one study,
472 Levy et al. (44) characterized two immune cell states with distinct expression patterns in adults of
473 the obligate symbiotic stony coral *Stylaphora pistillata*. In other studies, Hu et al. (45,65) described
474 how LePin, a lectin involved in phagocytic pathways of the cnidarian immune system, is required
475 for symbiont establishment in algal-hosting cells of the soft coral *Xenia* sp. Cell state-specific
476 regulation of the cnidarian immune system has also been proposed to occur in the sea anemone *E.*
477 *pallida* via whole-larvae fluorescence imaging and transcriptomics (66). Notably, MYD88, a
478 protein which transduces extracellular signals into the host to induce the NF-κB pathway (67,68),
479 is repressed in *E. pallida* algal-hosting cells; this local immune modulation only occurs in
480 symbiosis with compatible algae, thereby allowing host cells to sort and expel other non-symbiotic
481 microbes (66).

482 Our scRNA-seq approach highlights how the *O. arbuscula* immune system is
483 compartmentalized across cells and reveals how cell state-specific immune modulation may be
484 key to the maintenance of symbiosis in a host with a functional immune system. Here, one
485 population of gastrodermal cells hosts algal symbionts in symbiotic *O. arbuscula* by
486 downregulating select pathways in the innate immune system. Although we were unable to identify
487 LePin in our data, a clear signature of immunity downregulation was observed, which included
488 several Heat-Shock Proteins (46,48,49,54,69) and Cathepsins (50–52) that are also known to be
489 part of the NF-κB pathway. Interestingly, these genes have been previously shown to be markers
490 for immune cells in the stony coral *S. pistillata* (44), but it is not known whether this immune
491 signature in gastrodermal cells is conserved in cnidarians engaged in obligate symbioses.

492 Evidence for localized regulation of the NF-κB pathway in algal-hosting gastrodermal cells
493 has now been shown in a soft coral (65), a sea anemone (66), and a stony coral (this study). This

494 compartmentalized immune system regulation allows for the maintenance of whole-organism
495 immunity across other cell types, most notably in immune cells. We observed no differences in
496 gene expression in *O. arbuscula* Immune Cells between symbiotic and aposymbiotic tissues. The
497 maintenance of immunity function across other cell types in *O. arbuscula* in and out of symbiosis
498 provides nuance to the proposed immunity-nutrient tradeoff that symbiotic cnidarians must
499 balance: that is, in order that hosting algal symbionts is not be at the cost of whole-organism
500 immunity. The immune system can evolve in different ways across metazoans. For example, in
501 the three-spined stickleback *Gasterosteus aculeatus*, eight distinct immune cell states were
502 identified with distinct abundances and transcriptomic profiles across populations, demonstrating
503 specialized and rapid evolution of compartmentalized immune regulation (70). Here, we observe,
504 in a more basal metazoan and invertebrate, that "microevolution" of the immune system in *O.*
505 *arbuscula* has occurred in three transcriptomically distinct immune cell states and, notably, in a
506 specialized gastrodermal cell state, allowing these gastrodermal cells to function as pseudo-
507 immune cells without a cost to immune cell function. Notably, because canonical immune cells
508 should be able to maintain whole-organism immunity across symbiotic states, previous work
509 showing differences in pathogen susceptibility by symbiotic state observed in tropical corals in the
510 field (22,24) may be attributed to other factors (e.g., capacity for heterotrophy, efficiency of host-
511 algal nutrient exchange, etc.) and may not be due to baseline immune cell tradeoffs as a result of
512 symbiosis (25). However, additional work focused on characterizing differences between
513 immunity compartmentalization in obligate versus facultative cnidarians is necessary. Finally, the
514 attenuation of immune factors in the gastrodermal algal-hosting cells may represent a weak point
515 of entry for pathogen infection. Indeed, Stony Coral Tissue Loss Disease involves a breakdown of

516 symbiosis, and recent work has indicated that pathogens originating from the algal endosymbionts
517 may be responsible for this disease (71).

518 Our single-cell atlas also provides insights into carbon and nitrogen cycling within the
519 gastrodermal cells of symbiotic and aposymbiotic *O. arbuscula*. Notably, we find that the
520 gastrodermal cells where immunity is suppressed to allow for symbiosis are the same cells that
521 undergo active nutrient cycling, likely to regulate algal cell proliferation (6,13,72). Previous work
522 has proposed that increased nitrogen cycling and assimilation occurring in symbiotic host cells
523 controls algal cell proliferation to maintain optimal nutrient exchange between host and symbiont,
524 preventing parasitism of the symbiont on the host (6,12). In our data, the co-expression of sugar
525 transport and nitrogen cycling genes within the same (algal-hosting) cells supports recent work
526 showing that the stability of cnidarian-algal relationships relies on glucose-dependent nitrogen
527 competition between the host and symbiont (12). In this model, the metabolites and energy
528 produced from host glycolysis of symbiont-derived glucose are used by the host for amino acid
529 synthesis, through which nitrogen species (e.g., ammonium) can be assimilated. Hosts can thus
530 modulate the amount of ammonium translocated to the symbiont for proliferation (12). However,
531 here, gastrodermal cells from aposymbiotic tissue exhibited lower expression of sugar transport
532 and nitrogen cycling genes, which is likely driven by symbiotic cnidarians obtaining glucose
533 sugars from symbiotic algae, whereas aposymbiotic *O. arbuscula* rely on heterotrophic sources to
534 meet their metabolic needs (9,73). Thus, metabolic processing of carbon and nitrogen are likely
535 performed through distinct pathways in cnidarians that rely predominantly on heterotrophy (i.e.,
536 aposymbiotic corals) compared to those that rely predominantly on autotrophy (i.e., symbiotic
537 corals) (62).

538 Finally, while our 16S rRNA analysis revealed no differences in the composition or
539 diversity of the bacterial communities between symbiotic and aposymbiotic *O. arbuscula*,
540 microbial partners may still play a role in nutrient cycling and host immunity. Differences in
541 bacterial composition may not have been observed in our study because corals were housed in
542 common garden conditions. Future experiments with increased sample sizes collected *in situ*,
543 coupled with metabolomics or metatranscriptomics of the bacterial communities, would more fully
544 capture the functional variation of bacterial communities between symbiotic states.

545 Our scRNA-seq approach applied in a facultative coral provides a useful system to study
546 the cell and molecular processes associated with the cnidarian-algal symbiosis. Previous work
547 using whole-organism experimental techniques suggested that immunity costs are associated with
548 hosting algal symbionts (13,19). Herein, we showcase how differences in cell abundance and gene
549 expression can conflate patterns observed in whole-organism 'omics studies and, importantly,
550 facilitate compartmentalization of immune regulation to allow for endosymbiosis. We describe
551 highly specialized cell state-specific immune system regulation in a basal metazoan, highlighting
552 that the immune costs of symbiosis previously observed in whole organism studies might not be
553 as costly as previously assumed. Future work should explore how compartmentalized immunity is
554 modulated in different host-algal pairings in facultative and obligate cnidarians and determine how
555 these cellular processes are shaped by changing environmental conditions.

556

557 **Acknowledgements**

558 This research was supported by a National Science Foundation grant IOS-1937650 (to T.D.G. and
559 S.W.D.). M.V.-I. was supported by an NSF Graduate Research Fellowship and NSF NRT DGE
560 1735087. M.V.-I. And J.K.D.-A. were supported by Boston University Marine Program (BUMP)

Warren McLeod Marine Fellowships. We thank Diana Burkart-Waco of 10X Genomics Support for assistance with data processing. We also thank Boston University Microarray & Sequencing Resource Core Facility, the Boston University Single Cell Sequencing Core Facility, Boston University Shared Computing Cluster, and the Tufts University Core Facility.

Data availability

Raw fastq files for 16S and single-cell RNA-seq data can be found on NCBI's Short Read Archive Bioproject PRJNA1122932. All data and code for analyses can be found at https://github.com/mariaingersoll/Oculina_sc_manuscript.git.

Competing interests

The authors declare no competing interests.

REFERENCES

1. Thrall PH, Hochberg ME, Burdon JJ, Bever JD. Coevolution of symbiotic mutualists and parasites in a community context. Trends in Ecology & Evolution. 2007 Mar 1;22(3):120–6.
2. Baker DM, Freeman CJ, Wong JCY, Fogel ML, Knowlton N. Climate change promotes parasitism in a coral symbiosis. ISME Journal. 2018 Mar;12(3):921–30.
3. Lesser MP, Stat M, Gates RD. The endosymbiotic dinoflagellates (Symbiodinium sp.) of corals are parasites and mutualists. Coral Reefs. 2013 Sep 1;32(3):603–11.
4. Mansfield KM, Gilmore TD. Innate immunity and cnidarian-Symbiodiniaceae mutualism. Developmental & Comparative Immunology. 2019 Jan 1;90:199–209.
5. Zambrano-Villa S, Rosales-Borjas D, Carrero JC, Ortiz-Ortiz L. How protozoan parasites evade the immune response. Trends in Parasitology. 2002 Jun 1;18(6):272–8.
6. Xiang T, Lehnert E, Jinkerson RE, Clowez S, Kim RG, DeNofrio JC, et al. Symbiont population control by host-symbiont metabolic interaction in Symbiodiniaceae-cnidarian associations. Nature Communications. 2020 Jan 8;11(1):108.
7. Whittle M, Bonsall MB, Barreaux AMG, Ponton F, English S. A theoretical model for host-controlled regulation of symbiont density. Journal of Evolutionary Biology. 2023 Dec 1;36(12):1731–44.
8. Muscatine L, Cernichiari E. Assimilation of photosynthetic products of zooxanthellae by a reef coral. The Biological Bulletin. 1969 Dec;137(3):506–23.
9. Burriesci MS, Raab TK, Pringle JR. Evidence that glucose is the major transferred metabolite in dinoflagellate–cnidarian symbiosis. Journal of Experimental Biology. 2012 Oct 1;215(19):3467–77.
10. Lipschultz F, Cook C. Uptake and assimilation of 15N-ammonium by the symbiotic sea anemones *Bartholomea annulata* and *Aiptasia pallida*: conservation versus recycling of nitrogen. Marine Biology. 2002 Mar 1;140(3):489–502.
11. Yellowlees D, Rees TAV, Leggat W. Metabolic interactions between algal symbionts and invertebrate hosts. Plant, Cell & Environment. 2008;31(5):679–94.
12. Cui G, Liew YJ, Li Y, Kharbatia N, Zahran NI, Emwas AH, et al. Host-dependent nitrogen recycling as a mechanism of symbiont control in Aiptasia. PLOS Genetics. 2019 June 24;15(6):e1008189.
13. Rivera HE, Davies SW. Symbiosis maintenance in the facultative coral, Oculina arbuscula, relies on nitrogen cycling, cell cycle modulation, and immunity. Scientific Reports. 2021 Oct 27;11(1):21226.
14. Hoegh-Guldberg O. Coral reef ecosystems and anthropogenic climate change. Regional Environmental Change. 2011 Mar 1;11(1):215–27.
15. Bove CB, Ingersoll MV, Davies SW. Help me, symbionts, you're my only hope: approaches to accelerate our understanding of coral holobiont interactions. Integrative and Comparative Biology. 2022 Dec 1;62(6):1756–69.
16. Davy SK, Allemand D, Weis VM. Cell biology of cnidarian-dinoflagellate symbiosis. Microbiology and Molecular Biology Reviews. 2012 Jun 11;76(2):229–61.
17. Cui G, Konciute MK, Ling L, Esau L, Raina JB, Han B, et al. Molecular insights into the Darwin paradox of coral reefs from the sea anemone Aiptasia. Science Advances. 2023 Mar 15;9(11):eadf7108.
18. Gault JA, Bentlage B, Huang D, Kerr AM. Lineage-specific variation in the evolutionary stability of coral photosymbiosis. Science Advances. 2021 Sep 22;7(39):eabh4243.
19. Mansfield KM, Carter NM, Nguyen L, Cleves PA, Alshanbayeva A, Williams LM, et al.

Transcription factor NF-κB is modulated by symbiotic status in a sea anemone model of cnidarian bleaching. Scientific Reports. 2017 Nov 22;7(1):16025.

20. Matthews JL, Crowder CM, Oakley CA, Lutz A, Roessner U, Meyer E, et al. Optimal nutrient exchange and immune responses operate in partner specificity in the cnidarian-dinoflagellate symbiosis. Proceedings of the National Academy of Sciences USA. 2017 Dec 12;114(50):13194–9.
21. Stankiewicz KH, Guiglielmoni N, Kitchen SA, Flot JF, Barott KL, Davies SW, et al. Genomic comparison of the temperate coral Astrangia poculata with tropical corals yields insights into winter quiescence, innate immunity, and sexual reproduction. bioRxiv; 2023. p. 2023.09.22.558704.
22. Merselis DG, Lirman D, Rodriguez-Lanetty M. Symbiotic immuno-suppression: is disease susceptibility the price of bleaching resistance? PeerJ. 2018 Apr 17;6:e4494.
23. Muller EM, Bartels E, Baums IB. Bleaching causes loss of disease resistance within the threatened coral species *Acropora cervicornis*. eLife. 2018 Sep 11;7:e35066.
24. Shore-Maggio A, Callahan SM, Aeby GS. Trade-offs in disease and bleaching susceptibility among two color morphs of the Hawaiian reef coral, *Montipora capitata*. Coral Reefs. 2018 Jun 1;37(2):507–17.
25. Valadez-Ingersoll M, Aguirre Carrión PJ, Bodnar CA, Desai NA, Gilmore TD, Davies SW. Starvation differentially affects gene expression, immunity and pathogen susceptibility across symbiotic states in a model cnidarian. Proceedings of the Royal Society B: Biological Sciences. 2024 Feb 28;291(2017):20231685.
26. Changsut I, Womack HR, Shickle A, Sharp KH, Fuess LE. Variation in symbiont density is linked to changes in constitutive immunity in the facultatively symbiotic coral, *Astrangia poculata*. Biology Letters. 2022 Nov 16;18(11):20220273.
27. Lajeunesse TC, Parkinson JE, Reimer JD. A genetics-based description of *Symbiodinium minutum* sp. nov. and *S. psygmophilum* sp. nov. (Dinophyceae), two dinoflagellates symbiotic with cnidaria. Journal of Phycology. 2012;48(6):1380–91.
28. Enríquez S, Méndez ER, Inglesias-Prieto RI. Multiple scattering on coral skeletons enhances light absorption by symbiotic algae. Limnology and Oceanography. 2005;50(4):1025–32.
29. Scheufen T, Iglesias-Prieto R, Enríquez S. Changes in the number of symbionts and Symbiodinium cell pigmentation modulate differentially coral light absorption and photosynthetic performance. Frontiers in Marine Science. 2017 Sep 26;4.
30. Vásquez-Elizondo RM, Legaria-Moreno L, Pérez-Castro MÁ, Krämer WE, Scheufen T, Iglesias-Prieto R, et al. Absorptance determinations on multicellular tissues. Photosynthesis Research. 2017 Jun 1;132(3):311–24.
31. Parada AE, Needham DM, Fuhrman JA. Every base matters: assessing small subunit rRNA primers for marine microbiomes with mock communities, time series and global field samples. Environmental Microbiology. 2016;18(5):1403–14.
32. Apprill A, McNally S, Parsons R, Weber L. Minor revision to V4 region SSU rRNA 806R gene primer greatly increases detection of SAR11 bacterioplankton. Aquatic Microbial Ecology. 2015 Jun 4;75(2):129–37.
33. Oksanen J, Simpson GL, Blanchet FG, Kindt R, Legendre P, Minchin PR, et al. vegan: Community Ecology Package. 2024. Available from: https://cran.r-project.org/web/packages/vegan/index.html.
34. Love MI, Huber W, Anders S. Moderated estimation of fold change and dispersion for RNA-seq data with DESeq2. Genome Biology. 2014 Dec 5;15(12):550.

35. Aguirre Carrión PJ, Williams LM, Gilmore TD. Molecular and biochemical approaches to study the evolution of NF-κB signaling in basal metazoans. Methods in Molecular Biology. 2021 2366:67-91 I5.
36. Guo H, Isserlin R, Chen X, Wang W, Phanse S, Zandstra PW, et al. Integrative network analysis of signaling in human CD34+ hematopoietic progenitor cells by global phosphoproteomic profiling using TiO2 enrichment combined with 2D LC-MS/MS and pathway mapping. PROTEOMICS. 2013;13(8):1325–33.
37. Ying H, Cooke I, Sprungala S, Wang W, Hayward DC, Tang Y, et al. Comparative genomics reveals the distinct evolutionary trajectories of the robust and complex coral lineages. Genome Biology. 2018 Nov 2;19(1):175.
38. Blum BC, Emili A. Omics Notebook: robust, reproducible and flexible automated multiomics exploratory analysis and reporting. Bioinformatics Advances. 2021 Jan 1;1(1):vbab024.
39. Mering C von, Huynen M, Jaeggi D, Schmidt S, Bork P, Snel B. STRING: a database of predicted functional associations between proteins. Nucleic Acids Research. 2003 Jan 1;31(1):258–61.
40. Shannon P, Markiel A, Ozier O, Baliga NS, Wang JT, Ramage D, et al. Cytoscape: a software environment for integrated models of biomolecular interaction networks. Genome Research. 2003 Nov 1;13(11):2498–504.
41. Rosental B, Kozhekbaeva Z, Fernhoff N, Tsai JM, Traylor-Knowles N. Coral cell separation and isolation by fluorescence-activated cell sorting (FACS). BMC Cell Biology. 2017 Aug 29;18(1):30.
42. Zheng GXY, Terry JM, Belgrader P, Ryvkin P, Bent ZW, Wilson R, et al. Massively parallel digital transcriptional profiling of single cells. Nature Communications. 2017 Jan 16;8(1):14049.
43. Hao Y, Stuart T, Kowalski MH, Choudhary S, Hoffman P, Hartman A, et al. Dictionary learning for integrative, multimodal and scalable single-cell analysis. Nature Biotechnology. 2024 Feb;42(2):293–304.
44. Levy S, Elek A, Grau-Bové X, Menéndez-Bravo S, Iglesias M, Tanay A, et al. A stony coral cell atlas illuminates the molecular and cellular basis of coral symbiosis, calcification, and immunity. Cell. 2021 May 27;184(11):2973-2987.e18.
45. Hu M, Zheng X, Fan CM, Zheng Y. Lineage dynamics of the endosymbiotic cell type in the soft coral Xenia. Nature. 2020 Jun;582(7813):534–8.
46. DeSalvo MK, Sunagawa S, Voolstra CR, Medina M. Transcriptomic responses to heat stress and bleaching in the elkhorn coral Acropora palmata. Marine Ecology Progress Series. 2010 Mar 8;402:97–113.
47. Kenkel CD, Aglyamova G, Alamaru A, Bhagooli R, Capper R, Cunning R, et al. Development of gene expression markers of acute heat-light stress in reef-building corals of the genus Porites. PLOS ONE. 2011 Oct 26;6(10):e26914.
48. Kenkel CD, Sheridan C, Leal MC, Bhagooli R, Castillo KD, Kurata N, et al. Diagnostic gene expression biomarkers of coral thermal stress. Molecular Ecology Resources. 2014;14(4):667–78.
49. Cleves PA, Krediet CJ, Lehnert EM, Onishi M, Pringle JR. Insights into coral bleaching under heat stress from analysis of gene expression in a sea anemone model system. Proceedings of the National Academy of Sciences. 2020 Nov 17;117(46):28906–17.
50. Seth P, Mahajan VS, Chauhan SS. Transcription of human cathepsin L mRNA species hCATL B from a novel alternative promoter in the first intron of its gene. Gene. 2003 Dec 4;321:83–

91.
51. Sproles AE, Oakley CA, Matthews JL, Peng L, Owen JG, Grossman AR, et al. Proteomics quantifies protein expression changes in a model cnidarian colonised by a thermally tolerant but suboptimal symbiont. ISME Journal. 2019 Sep;13(9):2334–45.
52. Senjor E, Kos J, Nanut MP. Cysteine cathepsins as therapeutic targets in immune regulation and immune disorders. Biomedicines. 2023 Feb;11(2):476.
53. Soria-Valles C, Gutiérrez-Fernández A, Osorio FG, Carrero D, Ferrando AA, Colado E, et al. MMP-25 metalloprotease regulates innate immune response through NF-κB signaling. Journal of Immunology. 2016 Jul 1;197(1):296–302.
54. Ávila MF, Torrente D, Cabezas R, Morales L, García-Segura LM, Gonzalez J, et al. Structural insights from GRP78–NF-κB binding interactions: A computational approach to understand a possible neuroprotective pathway in brain injuries. Journal of Theoretical Biology. 2014 Mar 21;345:43–51.
55. Liu T, Zhang L, Joo D, Sun SC. NF-κB signaling in inflammation. Signal Transduction and Targeted Therapy. 2017 Jul 14;2(1):1–9.
56. Heyninck K, De Valck D, Berghe WV, Van Criekinge W, Contreras R, Fiers W, et al. The zinc finger protein A20 inhibits TNF-induced NF-κB–dependent gene expression by interfering with an RIP- or TRAF2-mediated transactivation signal and directly binds to a novel NF-κB–inhibiting protein ABIN. Journal of Cell Biology. 1999 Jun 28;145(7):1471–82.
57. Xie Z, Zhang M, Zhou G, Lin L, Han J, Wang Y, et al. Emerging roles of the Hedgehog signalling pathway in inflammatory bowel disease. Cell Death Discovery. 2021 Oct 26;7(1):1–9.
58. Chanchevalap S, Nandan MO, McConnell BB, Charrier L, Merlin D, Katz JP, et al. Krüppel-like factor 5 is an important mediator for lipopolysaccharide-induced proinflammatory response in intestinal epithelial cells. Nucleic Acids Research. 2006 Feb 1;34(4):1216–23.
59. Kumada K, Fuse N, Tamura T, Okamori C, Kurata S. HSP70/DNAJA3 chaperone/cochaperone regulates NF-κB activity in immune responses. Biochemical and Biophysical Research Communications. 2019 Jun 11;513(4):947–51.
60. Chou CW, Huang YK, Kuo TT, Liu JP, Sher YP. An Overview of ADAM9: structure, activation, and regulation in human diseases. International Journal of Molecular Sciences. 2020 Jan;21(20):7790.
61. He WA, Berardi E, Cardillo VM, Acharyya S, Aulino P, Thomas-Ahner J, et al. NF-κB–mediated Pax7 dysregulation in the muscle microenvironment promotes cancer cachexia. Journal of Clinical Investigation. 2013 Nov 1;123(11):4821–35.
62. Oakley CA, Ameismeier MF, Peng L, Weis VM, Grossman AR, Davy SK. Symbiosis induces widespread changes in the proteome of the model cnidarian Aiptasia. Cellular Microbiology. 2016;18(7):1009–23.
63. Lehnert EM, Mouchka ME, Burriesci MS, Gallo ND, Schwarz JA, Pringle JR. Extensive differences in gene expression between symbiotic and aposymbiotic cnidarians. G3 Genes|Genomes|Genetics. 2014 Feb 1;4(2):277–95.
64. Freedman AH, Sackton TB. Rethinking eco-evo studies of gene expression for non-model organisms in the genomic era. Molecular Ecology. 2024 May 9;n/a(n/a):e17378.
65. Hu M, Bai Y, Zheng X, Zheng Y. Coral–algal endosymbiosis characterized using RNAi and single-cell RNA-seq. Nature Microbiology. 2023 Jul;8(7):1240–51.
66. Jacobovitz MR, Rupp S, Voss PA, Maegele I, Gornik SG, Guse A. Dinoflagellate symbionts escape vomocytosis by host cell immune suppression. Nature Microbiology. 2021

757 Jun;6(6):769–82.
758 67. Sugiyama K ichi, Muroi M, Kinoshita M, Hamada O, Minai Y, Sugita-Konishi Y, et al. NF-
759 κB activation via MyD88-dependent Toll-like receptor signaling is inhibited by trichothecene
760 mycotoxin deoxynivalenol. Journal of Toxicological Sciences. 2016;41(2):273–9.
761 68. Gohda J, Matsumura T, Inoue J ichiro. Cutting edge: TNFR-associated factor (TRAF) 6 is
762 essential for MyD88-dependent pathway but not Toll/IL-1 receptor domain-containing
763 adaptor-inducing IFN-β (TRIF)-dependent pathway in TLR signaling. Journal of
764 Immunology. 2004 Sep 1;173(5):2913–7.
765 69. Ammirante M, Rosati A, Gentilella A, Festa M, Petrella A, Marzullo L, et al. The activity of
766 hsp90α promoter is regulated by NF-κB transcription factors. Oncogene. 2008
767 Feb;27(8):1175–8.
768 70. Fuess LE, Bolnick DI. Single-cell RNA sequencing reveals microevolution of the stickleback
769 immune system. Genome Biology and Evolution. 2023 Apr 1;15(4):evad053.
770 71. Work TM, Weatherby TM, Landsberg JH, Kiryu Y, Cook SM, Peters EC. Viral-like particles
771 are associated with endosymbiont pathology in Florida corals affected by Stony Coral Tissue
772 Loss Disease. Frontiers in Marine Science. 2021 Nov 5;8.
773 72. Rädecker N, Pogoreutz C, Voolstra CR, Wiedenmann J, Wild C. Nitrogen cycling in corals:
774 the key to understanding holobiont functioning? Trends in Microbiology. 2015 Aug
775 1;23(8):490–7.
776 73. Goldberg WM. Coral food, feeding, nutrition, and secretion: a review. Results and Problems
777 in Cell Differentiation. 2018 65:377-421.8.

778 **SUPPLEMENTARY FIGURES**

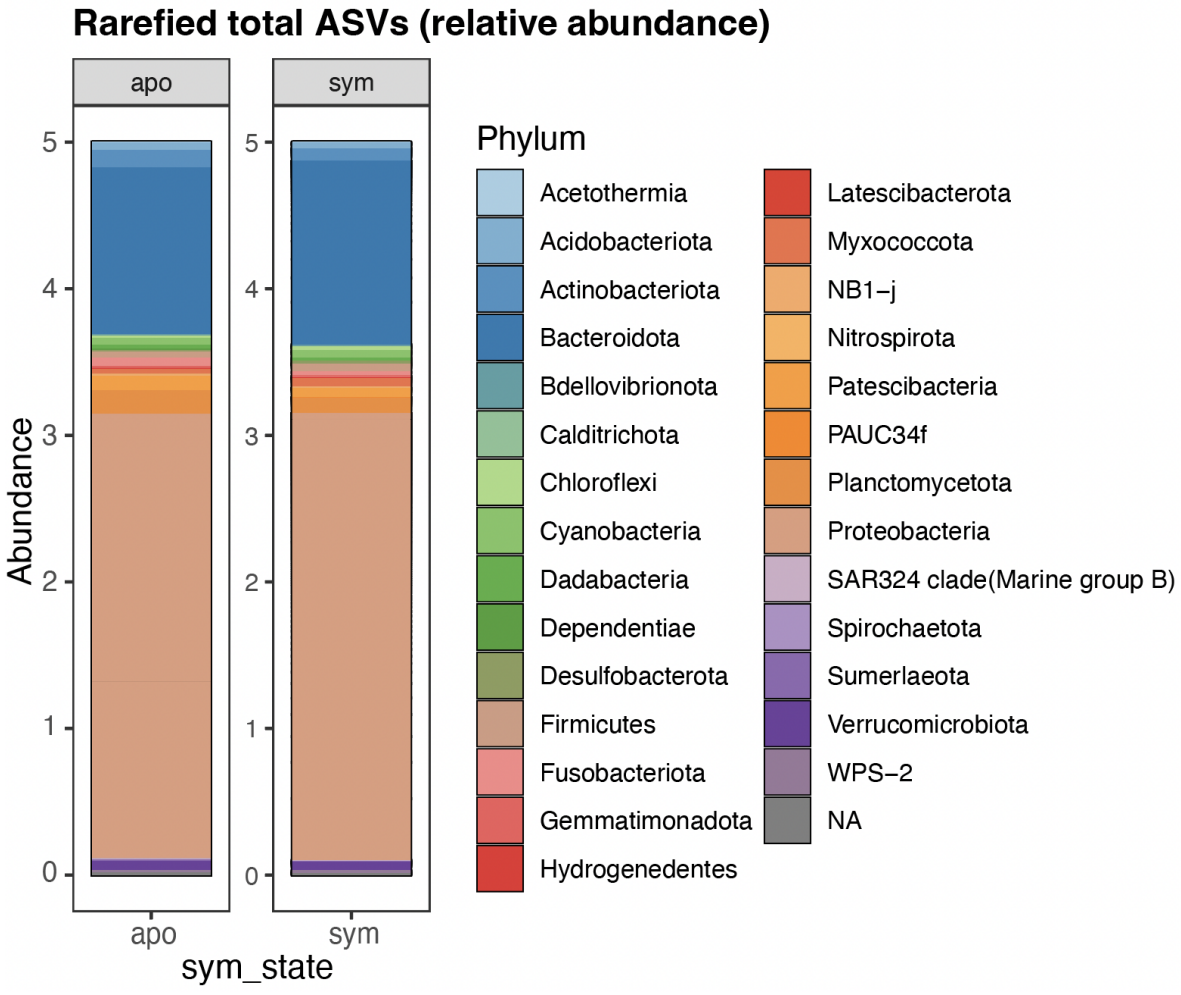

779

780 **Fig. S1. Similarity in bacterial communities by symbiotic state.** Relative abundance of 16S
781 ASVs from rarefied metabarcoding reads across different bacterial Phyla in symbiotic and
782 aposymbiotic *O. arbuscula*.

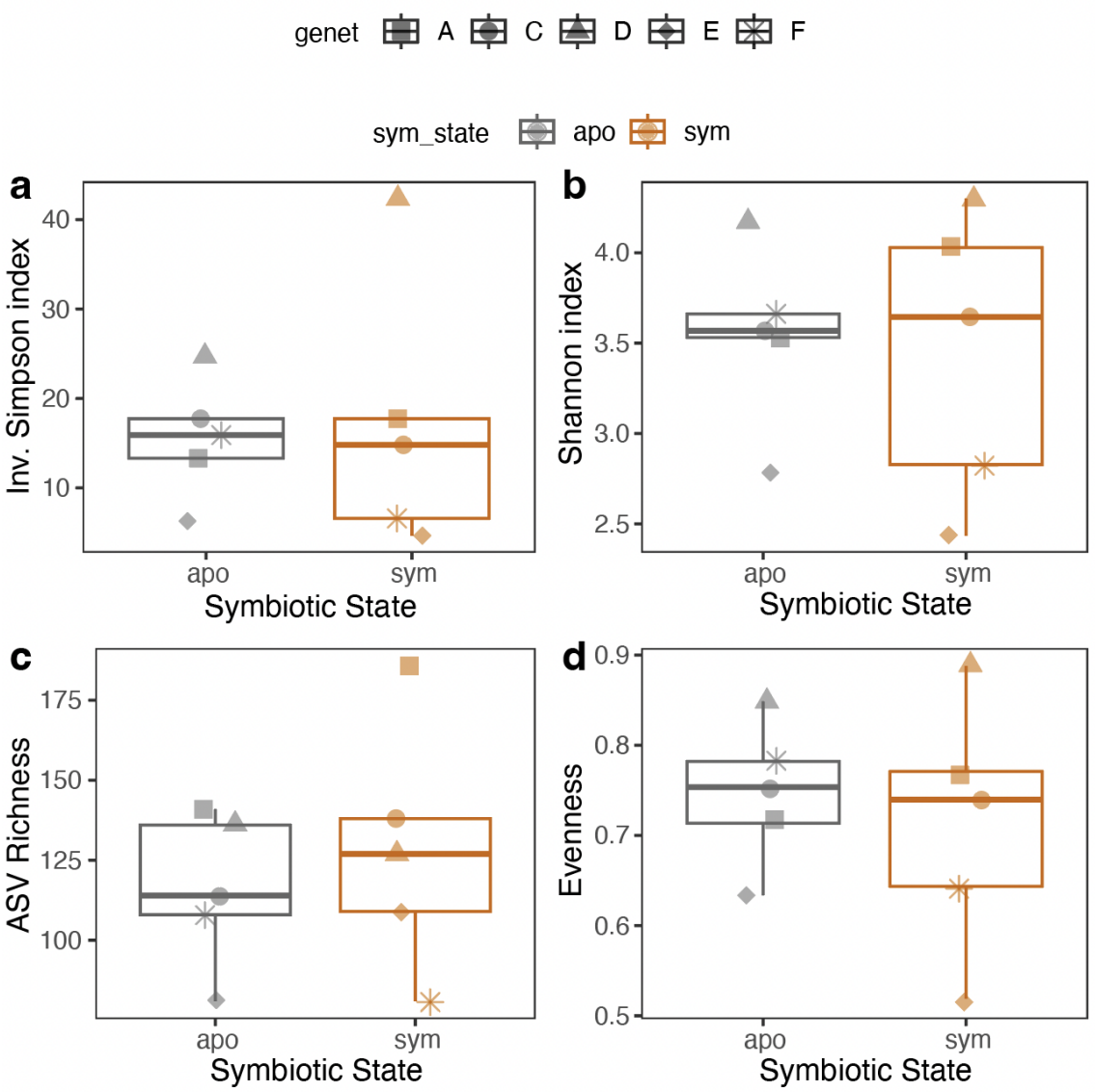

Figure S2. No differences in alpha diversity in the bacterial communities (16S rRNA metabarcoding) of symbiotic and aposymbiotic *O. arbuscula* (**a** Simpson Diversity; **b** Shannon Diversity, **c** Observed Species Richness from rarefied reads; **d** Evenness). Box plots display the median and the 1st and 3rd quartiles (hinges). Whiskers extend to the maximum and minimum points if they fall within 1.5 x the Interquartile Range (if no whiskers are drawn, points outside of the box are outliers). Each point is the alpha diversity metric of one individual (with the shape as genet).

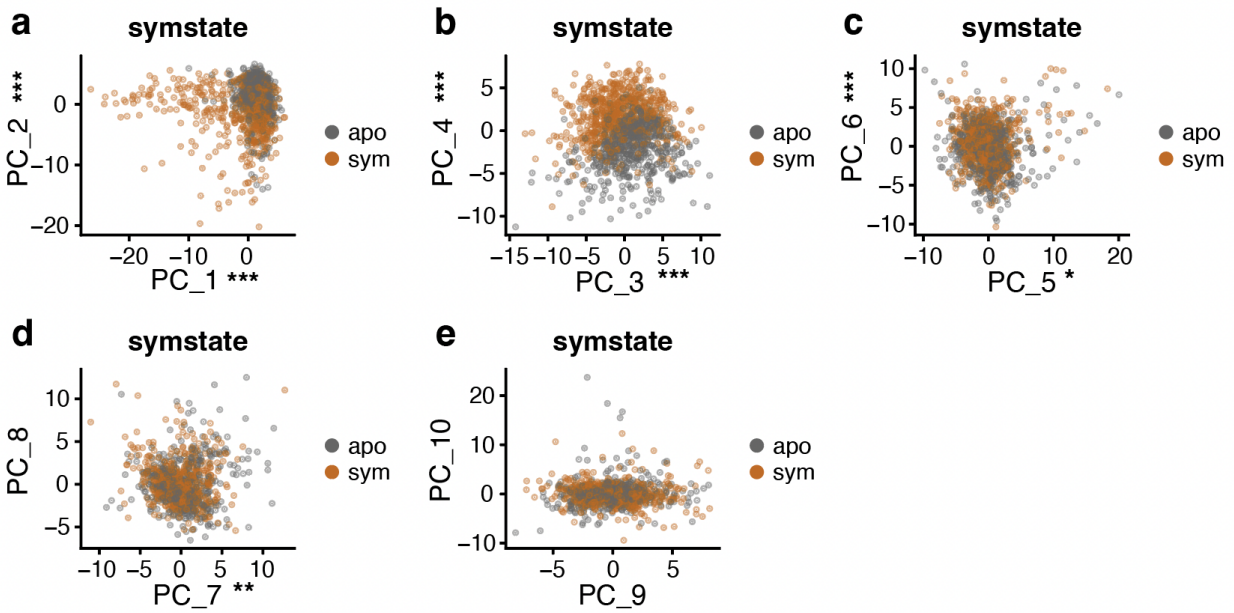

Figure S3. Gastrodermis 1 cells separate by symbiotic state along the first 7 PCs. Distribution of cells from the Gastrodermis 1 cluster from symbiotic (brown) and aposymbiotic (gray) *O. arbuscula* along Principal Components (PCs) 1-10 (**a** PC1 and PC2; **b** PC3 and PC4; **c** PC5 and PC6; **d** PC7 and PC8; **e** PC9 and PC10). Asterisks denote significant clustering of cells by symbiotic state along each PC (from analysis of variance; *** = *p*-value < 0.001, *** = *p*-value < 0.01, * = *p*-value < 0.05).

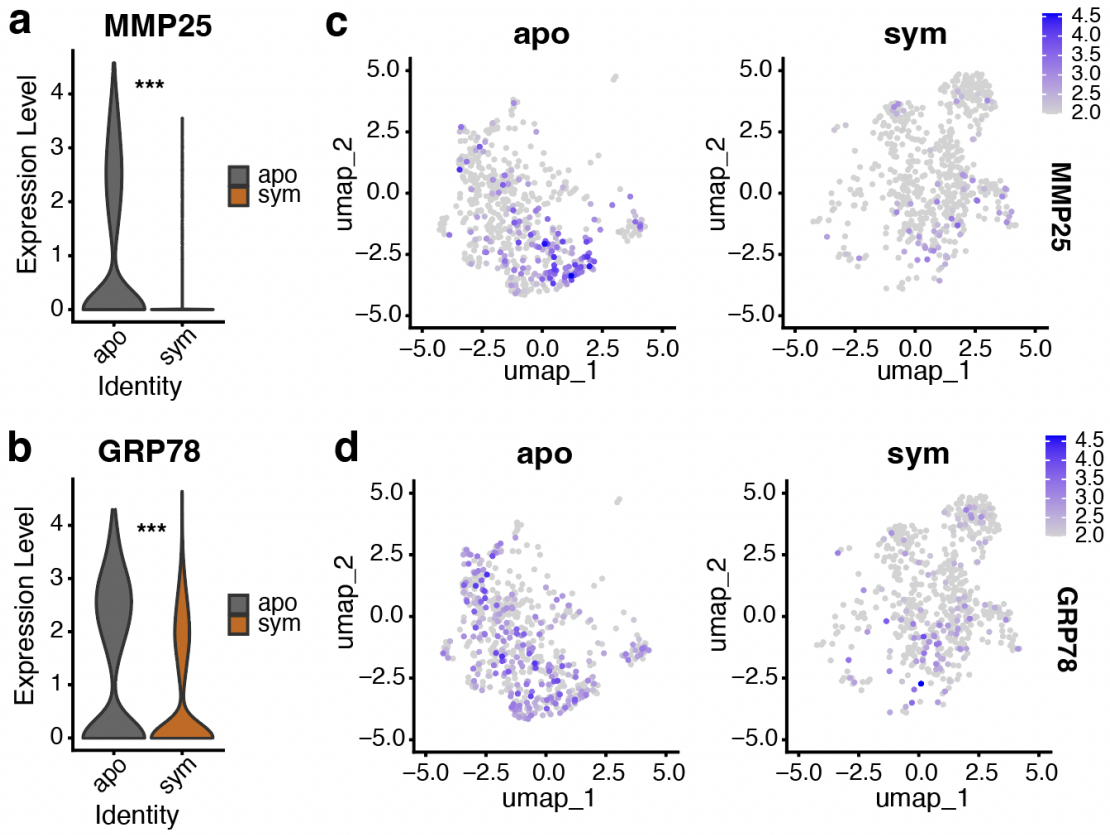

Figure S4. Immune genes are downregulated in symbiotic compared to aposymbiotic cells within the Gastrodermis 1 cluster. Putative NF-κB pathway genes Matrix Metallopeptidase 25 (MMP25 **a**) and Glucose-Regulated Protein 78 (GRP78 **b**) were more highly expressed in Gastrodermis 1 cells from aposymbiotic compared to symbiotic *O. arbuscula*. Expression levels of genes in **a-b** are normalized per cell, and significance is calculated from DESeq2 (*** = *p*-adjusted value < 0.001). Expression of MMP25 (**c**) and GRP78 (**d**) are plotted across all symbiotic and aposymbiotic Gastrodermis 1 cells. Coloration represents the normalized expression value (minimum normalized expression values plotted for MMP25 and GRP78 = 2).

808 **SUPPLEMENTARY TABLE**
809
810 **Table S1.** Raw and filtered read counts for samples used in 16S rRNA profiling (sym=symbiotic
811 and apo=aposymbiotic).
812

Sample	Sym State	Raw	Filtered
A13	Sym	21357	20430
A8	Apo	21478	20255
F8	Apo	10073	9138
F1	Sym	13139	12627
D7	Sym	14345	13561
D6	Apo	21389	20513
E8	Apo	13400	12994
E4	Sym	65019	63410
C6	Apo	14825	14102
C9	Sym	13305	11219

813

814 **SUPPLEMENTARY MATERIALS AND METHODS**

815 Detailed information on sample preparation, bioinformatic analyses, and R packages necessary to
816 complete the experiments outlined in the Materials and Methods section of the manuscript *Single-*
817 *cell RNA-sequencing reveals immune system compartmentalization under symbiosis in the stony*
818 *coral* Oculina arbuscula.

819

820 **Coral husbandry and manipulation of symbiotic state**

821 Symbiotic (in symbiosis with *Brevioulum psygmophilum*) (1) colonies from seven genetic
822 backgrounds (genets A-G) of *Oculina arbuscula* were collected at Radio Island Jetty, North
823 Carolina (34˚ 42.520' N, 76˚ 40.796' W) in May 2018 under NC Division of Marine Fisheries
824 Permit #1627488. These colonies have been maintained at Boston University in common garden
825 aquaria (25 °C (± 0.17, SD), 34.6 PSU (± 0.76, SD), pH 8.0 (± 0.08, SD)) since May, 2018. One
826 subset of aposymbiotic *O. arbuscula* branches was generated via menthol bleaching in Spring 2021
827 (symbiont counts, 16S metabarcoding, proteomics) and a second subset was generated in Spring
828 2022 (scRNAseq). Briefly, branches were incubated in 0.58 mM menthol in seawater under
829 common garden light conditions. The menthol solution was replaced every 24 h for a total of two
830 weeks. After aposymbiotic status was confirmed by a lack of symbiont autofluorescence under
831 fluorescence microscopy (Leica M165 FC), aposymbiotic branches were transferred back to
832 common garden aquaria and fragments were maintained for at least 2 months of recovery prior to
833 physiological and multiomic profiling.

834

835 **Tissue removal and symbiont cell quantification**

836 To measure symbiont cell densities hosted in branches of symbiotic and aposymbiotic *O.*
837 *arbuscula*, branches of approximately 2.5 cm in length were fragmented from symbiotic (N=10)
838 and aposymbiotic (N=10) samples from genets A, C, D, E, and F, with at least one sample per
839 genet for each symbiotic state. Tissue was removed via airbrushing into 0.2 µm-filtered Artificial
840 Seawater (Instant Ocean). Total volume was noted, the resulting tissue slurry was homogenized,
841 and an aliquot was subsampled for symbiont quantification using a hemocytometer. Skeleton
842 surface area was measured using an Einscan-SE scanner and MeshLab software and symbiont cells
843 were normalized to surface area. Statistical differences between symbiotic and aposymbiotic *O.*
844 *arbuscula* fragments were calculated using the Kruskal-Wallis rank sum test in Rstudio v4.3.0, as
845 assumptions of normality were not met.
846
847 **Coral spectroscopic determinations**
848 The light absorption capacity of symbiotic and aposymbiotic *O. arbuscula* was compared using
849 reflectance (R) and absorptance (A) (2–4). Coral reflectance (R), the fraction of light reflected by
850 the sample, was measured between 400-750 nm in intact coral fragments using a miniature
851 spectroradiometer (Flame-T-UV-Vis, Ocean Optics Inc.). Briefly, samples were placed in a black
852 container filled with filtered seawater and illuminated with homogeneous diffuse light by
853 positioning a semi-sphere with an internal reflecting coating (barium oxide BaO) above the
854 sample, and a ring of LEDs and halogen lamps directed upwards into the reflective coating. The
855 reflected light was collected by a 2 mm diameter fiber-optic that was placed 1 cm above the surface
856 of the sample at an angle of 45°. Reflectance was expressed as the ratio of the measurement from
857 the tissue surface relative to the reflectance of a coral reference (a bleached *O. arbuscula* skeleton
858 cleaned with commercial Hydrochloric Acid HCl). The coral absorptance (A), which describes the

859 fraction of incident light absorbed by the coral tissue, was calculated from the reflectance spectra
860 as A = 1 – R (2,4). The absorptance peak of chlorophyll a (Chl a) at 675 nm was calculated as A_{675}
861 = 1 – R_{675}, assuming that transmission through the skeleton of the samples is negligible.
862

863 **Microbiome profiling**

864 To identify bacterial communities associated with symbiotic and aposymbiotic fragments, one
865 symbiotic and one aposymbiotic fragment from genotypes A, C, D, E, and F were flash frozen,
866 and one polyp from each fragment was preserved in ethanol for 16S rRNA metabarcoding (N=10).
867 Metabarcoding libraries were generated using a series of PCR amplifications for the V4/V5 region
868 of the bacterial 16S rRNA gene (5,6) as follows: 95°C for 40 sec, 58°C for 120 sec, and 72°C for
869 60 sec for 32 cycles, with a final elongation step of 72°C for 5 min. PCR products were purified
870 using GeneJET PCR Purification kits (Thermo Fisher) and eluted in 30 µl. Each PCR product was
871 barcoded via five PCR cycles and visualized on a 1% agarose gel to assess relative concentrations.
872 Five negative controls using water were prepared and later used to remove contaminating
873 sequences. Samples were pooled in equal concentrations, gel extracted, and submitted for paired-
874 end 250 bp sequencing on an Illumina MiSeq at the Tufts University Core Facility.

875 16S primers were removed from raw reads using cutadapt (7). DADA2 v1.28.0 (8), quality
876 filtering was conducted, and 1,232 sequence variants (ASVs) were inferred. Taxonomy was
877 assigned at 100% sequence identity using the *Silva* v. 138.1 database (9). ASVs matching
878 mitochondria, chloroplasts, or non-bacterial kingdoms were removed (83 ASVs removed) and 20
879 ASVs were removed based on negative controls as contaminants (decontam v1.2.0; (10)). Cleaned
880 counts were rarefied to 8,298 using vegan v2.6-4 (11) and trimmed using MCMC.OTU v1.0.10
881 (12) to remove ASVs in less than 0.02% of counts, resulting in 661 ASVs across samples. The

882 composition of bacterial communities across symbiotic state were compared via alpha diversity
883 (Shannon index, Simpson's index, ASV richness, and evenness) using phyloseq v1.44.0 (function
884 *estimate_richness* (13)) and beta diversity was assessed using a PCoA on Bray–Curtis dissimilarity
885 with a PERMANOVA in the vegan package (v2.6-4 (11)). Alpha diversity metrics were compared
886 using linear mixed effects models ((package lme4; v1.1-35.3 (14)) with symbiotic state as the
887 predictor and a random effect of coral genotype. The effect of symbiotic state on beta diversity
888 was assessed using the function *betadisper* (vegan package; v2.6-4 (11)). DESeq2 v1.40.2 (15)
889 then explored differentially abundant ASVs to ensure that subtle differences in specific taxa were
890 not overlooked.
891
892 **Proteomic profiling**
893 Mass spectroscopy (MS) was used to identify differentially enriched proteins from total protein
894 isolated from fragments of five symbiotic genets (Ax2, C, E, and F) and three aposymbiotic genets
895 (C, E, and F). As described previously (16), each fragment (approximately 1 cm x 1 cm) was
896 washed in PBS then crushed and incubated in 1X AT Lysis buffer with proteinase inhibitors (10
897 mM HEPES pH 7.9, 1 mM EDTA, I mM EGTA, 20% w/v glycerol, 1% w/v Triton X-100, 20
898 mM NaF, 1 mM $Na_4P_2O_7 \cdot 10H_2O$, 1 mM dithiothreitol, 1 mM phenylmethylsulfonyl fluoride,
899 1 µg/ml leupeptin, 1 µg/ml pepstatin A, 10 µg/ml aprotinin) for 1 h at 4 ℃ on an orbital shaker with
900 occasional vortexing. The lysate was clarified by centrifugation at 13,000 rpm for 15 min at 4 ℃,
901 and the supernatant was stored at -80 ℃ prior to analysis by MS.
902 For MS, tryptic peptide mixtures were analyzed by nano-scale high-performance liquid
903 chromatography (Proxeon EASY-Nano system, Thermo Fisher Scientific) coupled with online
904 nanoelectrospray ionization tandem MS (Q-Exactive HF-X mass spectrometer; Thermo Fisher

905 Scientific). Briefly, samples were loaded into the system with aqueous 0.1% (v/v) formic acid via
906 a trap column (75 µm i.d. × 2 cm, Acclaim PepMap100 C18 3 µm, 100 Å, Thermo Fisher
907 Scientific) and peptides were resolved over an Easy-Spray analytical column (50 cm × 75 µm ID,
908 PepMap RSLC C18, Thermo Fisher Scientific) by an increasingly mobile phase B. comprising 2%
909 acetonitrile and 0.1% formic acid, while organic phase B consisted of 80% acetonitrile and 0.1%
910 formic acid. Reverse phase separation was performed over 120 min at a flow rate of 300 nl/min.
911 Eluted peptides were ionized directly into the mass spectrometer using a nanospray ion source.
912 The mass spectrometer was operated in positive ion mode with a capillary temperature of 300 °C
913 and a potential of 2,100 V applied to the frit. Tandem mass spectrometry (MS/MS) was performed
914 using high-energy collision-induced dissociation, and 10 MS/MS data-dependent scans (45,000
915 resolution) were acquired in profile mode alongside each profile mode full-scan mass spectra
916 (120,000 resolution), as previously described (17). For MS scans, the automatic gain control
917 (AGC) was set at 1×10^6 ions with a maximum fill time of 60 ms. MS/MS scans had an AGC of
918 3×10^4, with a maximum injection time of 80 msec, activation time of 0.1 msec, and 33%
919 normalized collision energy. To prevent repeated selection of peptides for MS/MS, a dynamic
920 exclusion list was activated to exclude all fragmented ions for 60 sec.

921 For protein identification and analysis, data files (RAW format) were searched using the
922 standard workflow of MaxQuant version 2.4 (http://www.maxquant.org/) under standard settings
923 using concatenated genomes of *Astrangia poculata* (18) and *Fungia* sp. (19). The parameters
924 included two missed trypsin cleavage sites, fixed carbamidomethylation of cysteine, variable
925 methionine oxidation, protein N-terminal acetylation, and phosphorylation of STY residues. For
926 the first search, precursor ion tolerances were set at 20 ppm, and for the second search, they were
927 set to 4.5 ppm. The MS/MS peaks were de-isotoped and searched using a 20-ppm mass tolerance.

928 A stringent false discovery rate (FDR) threshold of 1% was used to filter candidate peptides and
929 protein identifications. The searched intensity data were filtered, normalized, and clustered using
930 Omics Notebook (20). Filtering was performed to remove any proteins not identified in at least
931 70% of samples, with 2,730 proteins passing the filter. After filtering, both datasets showed low
932 levels of sparsity, and no missing value imputation was performed. The LIMMA R package was
933 used for LOESS normalization and differential abundance analysis (21). Differential analysis of
934 proteomic profiles between aposymbiotic and symbiotic samples was based on a moderated t-test
935 (20). Proteins were considered differentially abundant if they had a Bonferroni-adjusted p-value <
936 0.1. Raw intensity counts were normalized using the *rlog* transformation function in DESeq2 (15)
937 and visualized using a Principal Component Analysis (PCA) with the package vegan v2.6-4 (11).
938 The effects of symbiotic state and genet were assessed using PERMANOVA with the adonis2
939 function in vegan v2.6-4 (11).
940 Predicted peptides of *O. arbuscula* were searched against the human proteome v.11.5 from
941 the STRING v.11 database (22) with an e-value cut-off of $1x10^{-5}$. Protein–protein interactions of
942 select differentially expressed proteins (FDR < 0.1) were retrieved from the STRING v.11 database
943 (22). Interaction networks were visualized using Cytoscape v.3.7.2 (23).
944

945 **Single-cell RNA-sequencing**

946 To create single-cell libraries, one symbiotic (F1) and one aposymbiotic (F8) branch were sampled
947 for single-cell isolation and 10X cDNA sequencing, using a previously verified protocol for coral
948 cell isolation (24). Each fragment of approximately 1.5 cm in length was placed into 10 ml of ice-
949 cold calcium-free artificial seawater (0.2-micron filter-sterilized). The fragment was then moved
950 to 10 ml of ice-cold cell-isolation media (3.3x PBS, 2% heat-inactivated fetal bovine serum, 20

951 mM HEPES buffer in deionized H_2O). Using RNase-free forceps, tissue was mechanically scraped
952 from the skeleton until no visible tissue remained (<10 min). On ice, the cell-slurry was filtered
953 through a 70-µm filter, then through two 40-µm filters. This process was repeated for each sample.
954 1 ml of filtered cell suspension was centrifuged at 4°C for 10 min at 300 x g, and the pellet was
955 resuspended in 100 µl of cell-isolation media with 0.2 U/µl Protector RNase Inhibitor. Samples
956 were analyzed by the Boston University Single Cell Sequencing Core Facility where cell counts
957 and viability were quantified by 0.04% Trypan Blue staining and counting with a hemocytometer.
958 Symbiotic branch F1 had a concentration of 2,625 cells/µl and a viability of 81.6%. Aposymbiotic
959 branch F8 had a concentration of 3,312.5 cells/µl and a viability of 86.4%.

960 cDNA for each sample was generated following the 10X Genomics Chromium Single Cell
961 3'v3 protocols, and quality was assessed via Bioanalyzer High Sensitivity DNA analysis. Samples
962 were pooled in equimolar concentration, and the library was sequenced on an Illumina NextSeq
963 2000 (P3 100 kit) to obtain 50,000 reads per cell. 10X Genomics CellRanger (version 7.2.0 (25))
964 processed the sequencing reads, which were then aligned to the genome of *Astrangia poculata*
965 (18), which is closely related to *O. arbuscula*. Reads were mapped to a concatenated host
966 (*Astrangia poculata*) (18) and symbiont (*Breviolum psygmophilum*) (26) genome. Only reads
967 aligning confidently to the host reference were used to generate CellRanger output files.

968 To create cell profiles for *O. arbuscula* and assign cell state identities, host reads from
969 symbiotic and aposymbiotic samples were analyzed using Seurat (v.5.0.2) (27) in Rstudio
970 (v.4.2.3). Genes expressed in fewer than three cells were discarded, as were cells expressing fewer
971 than 200 genes. Datasets were first independently log-normalized, and the top 2000 genes that
972 exhibited high cell-to-cell variation were identified, expression values of these genes were scaled,
973 and a PCA was performed. To better identify cell clusters across both symbiotic states, the datasets

974 were integrated using the Canonical Correlation Analysis (CCA) Integration method on the PCA
975 reduction (nearest neighbors parameters). Clusters were identified using 30 dimensions and a
976 resolution of 0.5 and were visualized using Uniform Manifold Approximation and Projection
977 (UMAP). Marker genes were identified using FindAllMarkers (Wilcoxin Rank Sum Test; log-
978 fold-change threshold of 0.5) and compared to genes highly expressed in cell types from other
979 cnidarian single-cell datasets (28,29). 28 cell clusters across 6 cell types were identified in the
980 UMAP and were characterized using marker genes and previous scRNA-seq datasets in the corals
981 *Stylophora pistillata* (28) and *Xenia* sp. (29). Expression patterns of top marker genes were
982 assigned to cell clusters using violin plots, bubble plots, and visualization of gene expression in
983 individual cells within the UMAP. Next, the proportion of each cell cluster within each library was
984 calculated, which was defined by the number of cells in each cluster divided by the total number
985 of cells. Lastly, to assess the broad transcriptomic differences between each cell cluster, the top 10
986 genes enriched in each cell cluster (using the average log-2-fold-change from FindAllMarkers)
987 were identified.

988 To compare expression profiles of specific cell states between symbiotic and aposymbiotic
989 samples, cell clusters of interest were independently reclustered, and the effect of symbiotic state
990 on gene expression in each cell state was analyzed. First, the cell cluster of interest (*e.g.,* Immune
991 Cell, Gastrodermis 1) was subsetted from the full dataset, and new variable features were
992 identified. Data were then rescaled, and dimensionality reduction was re-run (using the first 30
993 dimensions). Subclusters were identified with resolutions of 0.5 (Immune Cell) and 0.25
994 (Gastrodermis 1). The distribution of cells across the subclusters according to the symbiotic state
995 was visualized using a UMAP. In Gastrodermis 1 and Immune Cell clusters, the proportion that
996 each subcluster represented from each library was calculated. Differentially expressed genes

997 between symbiotic states in the Immune Cell and Gastrodermis 1 cell clusters were identified using
998 the DESeq2 in the FindMarkers function. Additionally, marker genes for each subcluster were
999 identified. To highlight differences in the transcriptomes of the Immune Cell states, the top 20
1000 genes enriched in each Immune Cell subcluster were identified and plotted (unannotated genes
1001 were removed).

1002 To compare expression of genes involved in sugar transport and nutrient cycling between
1003 gastrodermal cells from symbiotic and aposymbiotic samples, the expression of sugar transport
1004 and nitrogen cycling genes in the reclustered Gastrodermis 1 cells was analyzed. Using VlnPlot,
1005 normalized differential expression values of genes involved in nitrogen cycling/symbiont density
1006 control (Glutamate Dehydrogenase DHE4 and Glutamate Synthase [NADH] GLSN) and sugar
1007 transport (Apolipophorin APOB.1) – identified in previous whole-organism RNA-seq studies (26)
1008 – between symbiotic and aposymbiotic cells were plotted across each of the subclusters of
1009 Gastrodermis 1. FeaturePlot was then used to visualize the co-expression of these genes across the
1010 subclusters of Gastrodermis 1 cells from the symbiotic sample (scaling the per-cell mean
1011 expression value of each gene to a maximum value of 10).

1012 Finally, to identify the genes driving separation across symbiotic state within Gastrodermis
1013 1, the distribution of Gastrodermis 1 cells was visualized along the first 10 Principal Components
1014 (PCs) of the PCA assay that were used to define the Gastrodermis 1 UMAP. An analysis of
1015 variance was used to determine whether the Gastrodermis 1 cells separated by symbiotic state
1016 (symbiotic vs. aposymbiotic) along each PC. The top 20 genes driving the distribution of cells
1017 along the first 7 PCs (10 genes driving each PC in the positive direction and 10 genes driving each
1018 PC in the negative direction) were selected, and unannotated genes were removed for a total of 86
1019 remaining genes. DESeq2 log2foldchange values for each of these genes were plotted in a bar

1020 graph, noting significantly differentially expressed genes (p-adjusted values < 0.05) and genes
1021 hypothesized to be involved in the NF-κB pathway. Normalized differential expression values of
1022 Heat Shock Factor 90 (H90A1), Cathepsin L (CATL.6), Cathepsin Z (CATZ), Matrix
1023 Metallopeptidase 25 (MMP25), and Glucose-Regulated Protein 78 (GRP78) were compared
1024 between symbiotic and aposymbiotic cells in Gastrodermis 1 using violin plots. The distribution
1025 of these genes across Gastrodermis 1 cells from symbiotic and aposymbiotic samples was further
1026 visualized to emphasize the reduction in certain immune pathways in predicted algal-hosting cells
1027 (FeaturePlot; minimum normalized expression value plotted for H90A1=3, and minimum
1028 normalized expression value plotted for CATL.6, CATZ, MMP25, and GRP78=2).

Supplementary References:

1. Lajeunesse TC, Parkinson JE, Reimer JD. A genetics-based description of *Symbiodinium minutum* sp. nov. and *S. psygmophilum* sp. nov. (Dinophyceae), two dinoflagellates symbiotic with cnidaria. Journal of Phycology. 2012;48(6):1380–91.
2. Enríquez S, Méndez ER, -Prieto RI. Multiple scattering on coral skeletons enhances light absorption by symbiotic algae. Limnology and Oceanography. 2005;50(4):1025–32.
3. Scheufen T, Iglesias-Prieto R, Enríquez S. Changes in the number of symbionts and symbiodinium cell pigmentation modulate differentially coral light absorption and photosynthetic performance. Frontiers in Marine Science. 2017 Sep 26;4.
4. Vásquez-Elizondo RM, Legaria-Moreno L, Pérez-Castro MÁ, Krämer WE, Scheufen T, Iglesias-Prieto R, et al. Absorptance determinations on multicellular tissues. Photosynthesis Research. 2017 Jun 1;132(3):311–24.
5. Parada AE, Needham DM, Fuhrman JA. Every base matters: assessing small subunit rRNA primers for marine microbiomes with mock communities, time series and global field samples. Environmental Microbiology. 2016;18(5):1403–14.
6. Apprill A, McNally S, Parsons R, Weber L. Minor revision to V4 region SSU rRNA 806R gene primer greatly increases detection of SAR11 bacterioplankton. Aquatic Microbial Ecology. 2015 Jun 4;75(2):129–37.
7. Martin M. Cutadapt removes adapter sequences from high-throughput sequencing reads. EMBnet Journal. 2011 May 2;17(1):10–2.
8. Callahan BJ, Sankaran K, Fukuyama JA, McMurdie PJ, Holmes SP. Bioconductor Workflow for Microbiome Data Analysis: from raw reads to community analyses. F1000Research. 2016 Nov 2;5:1492.
9. Quast C, Pruesse E, Yilmaz P, Gerken J, Schweer T, Yarza P, et al. The SILVA ribosomal RNA gene database project: improved data processing and web-based tools. Nucleic Acids Research. 2013 Jan 1;41(D1):D590–6.
10. Davis NM, Proctor DM, Holmes SP, Relman DA, Callahan BJ. Simple statistical identification and removal of contaminant sequences in marker-gene and metagenomics data. Microbiome. 2018 Dec 17;6(1):226.
11. Oksanen J, Simpson GL, Blanchet FG, Kindt R, Legendre P, Minchin PR, et al. vegan: Community Ecology Package 2024.
12. Matz MV. MCMC.OTU: Bayesian Analysis of Multivariate Counts Data in DNA Metabarcoding and Ecology. 2016.
13. McMurdie PJ, Holmes S. phyloseq: An R Package for Reproducible Interactive Analysis and Graphics of Microbiome Census Data. PLOS ONE. 2013 Apr 22;8(4):e61217.
14. Bates D, Mächler M, Bolker B, Walker S. Fitting Linear Mixed-Effects Models Using lme4. Journal of Statistical Software. 2015 Oct 7;67:1–48.
15. Love MI, Huber W, Anders S. Moderated estimation of fold change and dispersion for RNA-seq data with DESeq2. Genome Biology. 2014 Dec 5;15(12):550.
16. Aguirre Carrión PJ, Williams LM, Gilmore TD. Molecular and biochemical approaches to study the evolution of NF-κB signaling in basal metazoans. Methods in Molecular Biology 2021 2366:67-91.
17. Guo H, Isserlin R, Chen X, Wang W, Phanse S, Zandstra PW, et al. Integrative network analysis of signaling in human CD34+ hematopoietic progenitor cells by global phosphoproteomic profiling using TiO2 enrichment combined with 2D LC-MS/MS and

pathway mapping. PROTEOMICS. 2013;13(8):1325–33.

18. Stankiewicz KH, Guiglielmoni N, Kitchen SA, Flot JF, Barott KL, Davies SW, et al. Genomic comparison of the temperate coral *Astrangia poculata* with tropical corals yields insights into winter quiescence, innate immunity, and sexual reproduction. bioRxiv; 2023.
19. Ying H, Cooke I, Sprungala S, Wang W, Hayward DC, Tang Y, et al. Comparative genomics reveals the distinct evolutionary trajectories of the robust and complex coral lineages. Genome Biology. 2018 Nov 2;19(1):175.
20. Blum BC, Emili A. Omics Notebook: robust, reproducible and flexible automated multiomics exploratory analysis and reporting. Bioinformatics Advances. 2021 Jan 1;1(1):vbab024.
21. Ritchie ME, Phipson B, Wu D, Hu Y, Law CW, Shi W, et al. limma powers differential expression analyses for RNA-sequencing and microarray studies. Nucleic Acids Research. 2015 Apr 20;43(7):e47.
22. Mering C von, Huynen M, Jaeggi D, Schmidt S, Bork P, Snel B. STRING: a database of predicted functional associations between proteins. Nucleic Acids Research. 2003 Jan 1;31(1):258–61.
23. Shannon P, Markiel A, Ozier O, Baliga NS, Wang JT, Ramage D, et al. Cytoscape: a software environment for integrated models of biomolecular interaction networks. Genome Research. 2003 Nov 1;13(11):2498–504.
24. Rosental B, Kozhekbaeva Z, Fernhoff N, Tsai JM, Traylor-Knowles N. Coral cell separation and isolation by fluorescence-activated cell sorting (FACS). BMC Cell Biology. 2017 Aug 29;18(1):30.
25. Zheng GXY, Terry JM, Belgrader P, Ryvkin P, Bent ZW, Wilson R, et al. Massively parallel digital transcriptional profiling of single cells. Nature Communications. 2017 Jan 16;8(1):14049.
26. Rivera HE, Davies SW. Symbiosis maintenance in the facultative coral, Oculina arbuscula, relies on nitrogen cycling, cell cycle modulation, and immunity. Scientific Reports. 2021 Oct 27;11(1):21226.
27. Hao Y, Stuart T, Kowalski MH, Choudhary S, Hoffman P, Hartman A, et al. Dictionary learning for integrative, multimodal and scalable single-cell analysis. Nature Biotechnology. 2024 Feb;42(2):293–304.
28. Levy S, Elek A, Grau-Bové X, Menéndez-Bravo S, Iglesias M, Tanay A, et al. A stony coral cell atlas illuminates the molecular and cellular basis of coral symbiosis, calcification, and immunity. Cell. 2021 May 27;184(11):2973-2987.e18.
29. Hu M, Zheng X, Fan CM, Zheng Y. Lineage dynamics of the endosymbiotic cell type in the soft coral Xenia. Nature. 2020 Jun;582(7813):534–8.